The Influence of Microstructure on the Fatigue Crack Growth Rate in ferrite-pearlite Steels in the Paris Region

Victor Igwemezie[1], Ali Mehmanparast[1], and Feargal Brennan[2]

[1]Cranfield University
[2]University of Strathclyde

April 28, 2020

Abstract

This paper presents a study on the effect of microstructure on the fatigue crack growth rate (FCGR) in advanced normalised-rolled (NR) and thermomechanical control process (TMCP) S355 steels in the Paris Region of the da/dN vs. ΔK log-log plot. The environments of study were air and seawater (SW), under constant amplitude sinewave fatigue loading. Discussions were based mainly on the comparison between the crack path in the TMCP and NR steels. Fundamentally, three phenomena: crack-tip diversion, crack-front bifurcation and metal crumb formation were observed to influence the rate of fatigue crack growth (FCG). The prevalence of these phenomena appears to be a function of the nature of the material microstructure, environment and crack-tip loading conditions. The three factors appear to retard the crack growth by reducing or re-distributing the effective driving force at the main active crack tip. A crack path containing extensively the three phenomena was observed to offer strong resistance to FCG. Increase in the FCGR was observed with decrease in the crack-tip diversion angle, branched-crack length and metal crumbs formed. In SW, the degree of the electrochemical dissolution of the microplastic zone (or crack-tip blunting) appears to be an additional factor influencing crack growth in ferrite-pearlite (α-P) steel. This study, generally tends to present microstructural features that strongly influenced FCGR in α-P steels in the Paris Region both in air and SW. This work is very important in the design of fatigue resistant steel.

Posted on Authorea 13 Apr 2020 — CC BY 4.0 — https://doi.org/10.22541/au.158679911.16268490 — This a preprint and has not been peer reviewed. Data may be preliminary.

Introduction

Understanding how a crack propagates in a given material is fundamental to all forms of theoretical postulations, modelling, analytical and numerical analyses. If the premise of crack growth path is wrong, no matter how elegant the mathematical or numerical expression may appear, the result will not represent reality. The knowledge of corrosion fatigue and its mechanism is of immense value in preventing failure in marine environment. Understanding the influence of microstructure on fatigue mechanism is fundamental because it supports: fatigue life prediction of structures, design of fatigue resistant materials and realistic fatigue modelling attempts. Fatigue is a complex problem and there have been several numbers of publications on the problem of fatigue, each presenting similar or different ideas or trying to modify existing theories – using from simple to complex analytical and numerical approaches. Generally, fatigue crack growth (*FCG*) in metallic materials is divided into three regions. Each region has been reported to exhibit different mechanisms and characteristics. These regions are the threshold region (or early stages of fatigue crack development), the Paris Region (or the linear and steady crack growth stage) and region of final failure (or unstable/accelerated crack growth stage). The Paris Region is of interest in this study because it is the part commonly used and recommended in ASTM E647-15 [1] and BS EN ISO 11782-2:2008 [2] for engineering design.

In many reports [3][4][5][6][7][8], microstructure, mean stress, mechanical properties and initial crack length were said to have large influence on the threshold and final failure regions. In addition, the accelerated region is said to be influenced by sample thickness. These factors were reported to have little or negligible effects when the propagating crack has grown to a considerable length or beyond few grains, usually in the Paris Region [5][9][10][11][12][13][14]. In the threshold region, non-continuum or single shear mechanism is said to operate and the nature of the fractured surface is seen to be faceted. The crack tip was under both tensile and shear forces. The crack closure phenomenon was reported to be high and the plastic zone size is equal or less than the microstructural grain diameter. In the final or accelerated failure region, fatigue and additional static loading modes are said to operate. And, microvoid coalescence, intergranular or additional cleavage failure mechanism have been found on the fractured surface and the crack tip was under tensile loading. The plastic zone size in this final region was reported to be very much bigger than the grain diameter.

Many researchers have reported that fatigue failure in the Paris Region is generally by transgranular ductile striation mechanism [10][15][16]. The crack path is generally taken to be across the grains (or transcrystalline), although they may also propagate along the grain boundaries or intergranular depending on the material properties, loading and environmental conditions [17]. In this linear crack growth region, the crack tip is under tensile loading and the plastic zone size is reported to be greater than a grain diameter. The crack closure is low and mechanism of growth is by striation – alternating or simultaneous shear on two slip systems [16]. The conclusions [3][5][6][18] that microstructure has little or no influence on the fatigue crack growth rate ($FCGR$) of metallic materials is often based on the frequent observation of ductile striation mechanism in the Paris Region in fractographs. One thing that must be noted is that most of the fatigue theories existing today – including that of crack extension [16], crack path [15] and crack closure [19][20] were propounded from experiments performed on non-ferrous materials. For example, two other phenomena which are associated with crack retardation across metallic materials in the literature are crack closure and interlocking. It is pertinent to note that crack closure effect may be more important for non-ferrous ductile metals. It is a common knowledge that the concept of crack closure and the use of effective stress intensity factor range ($SIFR$) was proposed by Elber [19][20]. This theory is based on the fact that plastically deformed surface wake is left behind as the crack propagates. He argued that there is a premature contact of the crack faces during unloading from tension in a fatigue test. This effect reduces the effective stress at the crack tip. Elber proposed the use of effective $SIFR$ instead of the conventional $SIFR$ in plotting fatigue curve. The mechanisms such as the plasticity-induced and the roughness-induced crack closure can cause retardation of the$FCGR$. However, it is pertinent to note that Elber's theory is based on his study of 2024-T3 aerospace aluminium alloy of a moderate ductility. The validity of this theory to steel will vary since; (a) steel can have high ductility in annealed or fine-grained condition to 'near-brittle' ductility in martensitic or very low temperature condition, and (b) the thickness effect in steel material. As sample thickness of steel is increased, the plain stress region at the outer surface tends to be eliminated leaving only plain strain condition where plastic zone becomes little or almost negligible. Hence, the concept of crack closure may not be rigorously applied to steel at all conditions, coupled with the fatigue test condition under plain strain condition – i.e. with little or negligible plastic zone at the crack tip. In other words, when the plastic zone is little, the effect of crack closure can then be ignored, or its consequences will be insignificant.

None of these studies in practical terms showed vividly how the crack propagated through the phases in the microstructure of the materials studied. There are many variables, e.g. alloying elements and their concentrations, forming process and the mode of deformation, heat treatment - involving temperature range, heating time, cooling time, etc. which can be combined in so many ways to obtain varieties of steel properties, e.g., ranging from high ductility to almost completely brittle steel. The primary goal of this paper, therefore, is to present some observed microstructural influence on the FCG phenomenon in the Paris Region of ferrite-pearlite (α-Π) steels produced by Normalized-rolled (NR) and Thermo-mechanical control process ($TMCP$) in air and seawater (SW).

Posted on Authorea 13 Apr 2020 — CC BY 4.0 — https://doi.org/10.22541/au.158679911.16268490 — This a preprint and has not been peer reviewed. Data may be preliminary.

Metallurgy and characterisation of phase constituents of experimental steels

The increasing demand for economic steels with higher toughness, better weldability and less expensive alloying elements has resulted to modern *TMCP* steels. These materials are increasingly being used in the design of offshore support structures. Some of the advance structural steels are shown in Table 1(a) and conventional steels in Table 1(b). The *TMCP* steel grades have been manufactured specifically for offshore pipelines, platforms, pressure vessels, and modern wind turbine installations [21]. Currently they are replacing the more traditional ones in Table 1(b). The BS4360 Grade 50D is equivalent to S355J2+N hot rolled normalized steel.

Table 1: (a) Advanced S355 steel subgrades for marine applications [22] (b) Conventional S355 structural steel grades [23][24][25][26]

Offshore Structural Steel Plates	Offshore Structural Steel Plates	Offshore Structural Steel Plates
(a)	(a)	(b)
European	Typical offshore application	European
EN10225		EN10025 Part 2: 2004
S355G7+N	Primary Structure	S355
S355G7+M	Primary Structure	S355JR
S355G8+N	Critical Joints	S355JO
S355G8+M	Critical Joints	S355J2
S355G9+N	Primary Structure	S355J2+N
S355G9+M	Primary Structure	S355K2
S355G10+N	Critical Joints	S355K2+N
S355G10+M	Critical Joints	S355NL

Fig. 1(a) is common *Fe-C* phase diagram showing important regions in the heat treatment of marine steels. γ denotes austenite, αferrite and P pearlite. A_1 is an equilibrium lower transformation temperature. Eutectoid reaction occurs at A_1 which is 723*C in the binary diagram. The Ar_1 temperature depicts the lower transformation temperature upon cooling. Ac_1 temperature depicts the start point of the transformation between the α-ferrite and the austenite γ upon heating. A_3 is an equilibrium upper transformation temperature where alpha iron (α-$\Phi\epsilon$) transforms to gamma iron (γ-Fe) and it is 910°C for pure iron and it is lowered with addition of carbon. Ar_3 is the temperature at which austenite γ starts transforming to ferrite α during cooling. Ac_3 temperature depicts the upper transformation temperatures upon heating. The line in Fig. 1(a) are straight - in fact in the case above they are drawn arbitrarily. In reality, the shape and position of the lines – straight or curved, depend on the steel chemistry, cooling rate and rolling or deformation variables. Austenitization is the first operation in many of the most important deformation and heat treatment processes. After austenitization, upon cooling the austenite decomposes into various morphologies. From the austenite region, the bcc α-ferrite is reported to be the first to nucleate at the austenite grain surfaces. Other microstructures that form as the transformation temperature is lowered are pearlite (P), bainite, and martensite.

The nature of α-Πmicrostructure due to heat treatment can be explained by the type of heat treatment process – commonly referred to as as-rolled (AR), normalized (N), normalized-rolled (NR), quenched and tempered ($Q\&T$) and thermomechanical control process ($TMCP$). The common phases in these steels are ferrite (α) and pearlite ($\alpha+\Phi\epsilon_3$ˆ). Fig. 1(b - f) are schematic of heat treatment of modern steel. The heat treatments of interest in this study are AR , N , NR and$TMCP$. *Normalizing* involves cooling of austenitized steel, usually in air, to a temperature substantially below the transformation range [27]. The austenitizing temperature for normalizing is typically 30–80ºC above the Ac_3 transformation temperature

Posted on Authorea 13 Apr 2020 — CC BY 4.0 — https://doi.org/10.22541/au.158679911.16268490 — This a preprint and has not been peer reviewed. Data may be preliminary.

(the upper critical temperature, 800 – 925) for hypoeutectoid steels. As-rolled is obtained by austenitizing at say about 1250 °C, holding for specified time and then deforming at roughing and finishing mills within the austenite range. The finishing rolling may, for example, be at some temperature above Ac_3 and the steel is allowed to cool naturally to room temperature as shown in Fig. 1(b).

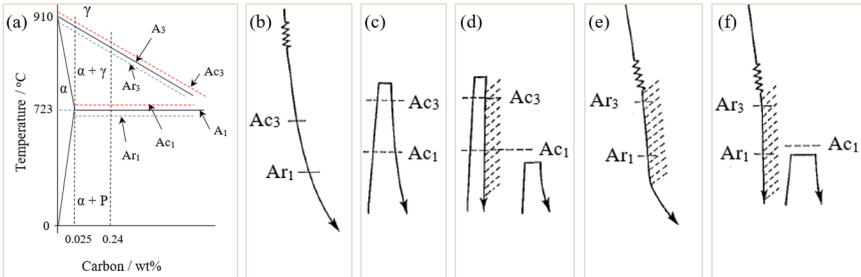

Fig. 1: Heat treatments of modern steel. (a) a schematic phase diagram of carbon composition range and phases expected in the microstructure of marine steel, (b & c) rolling and normalization (d) TMCP route involving reheating, accelerated cooling and self-temper or tempering at temperature below Ac_1 (e) rolling, accelerated cooling and (f) rolling, direct-quenching and tempering at temperature below Ac_1 [28][29].

Normalized steel (N -steel) is commonly obtained when the as-rolled steel is reheated to about 900°C or very little above Ac_3, held for a desired period and allowed to cool naturally back to room temperature as shown in Fig. 1(c). When the finishing rolling operation is done at a temperature above about 900°C before cooling naturally to room temperature, aNR -steel is obtained. Here no reheating is necessary. Normalized and NR steels have practically the same properties and so are designated 'N '. The strength or other properties of the steel can be increased by addition of small amount of alloying elements and then quenched or accelerated-cooled and tempered as shown in Fig. 1(d). The tempering is then done below Ac_1. $TMCP$ is a microstructural control technique combining controlled rolling (CR) and accelerated cooling to obtain exceptional strength-toughness combinations in low-alloy steels by grain refinement [29][30][31][32]. In general, controlled-rolling, controlled-cooling, accelerated cooling and direct-quenching are typical examples of thermomechanical processing [29]. Controlled rolling involves carrying out of the finishing deformation at temperature sufficiently low to prevent grain growth of the recrystallized austenite during cooling. The property obtained may not be different from those obtained after normalization [28][29]. The $TMCP$ route is illustrated in Fig. 1(e & f) [28]. Traditional marine steels shown in Table 1(b) are produced byAR , N or NR . The $TMCP$ steels production route is proprietary and so processing conditions and number of deformations are slightly different, producing what may appear as variation in the α and P sizes and morphologies.

Ideally, most common marine steels have microstructures consisting of very small volume fraction of P in a α matrix. It may be called α-Π steels where volume fraction of P phase is significant. The common α morphologies are grain boundary allotriomorphic α , idiomorphic α , Widmanstätten α , and intragranular α or acicular α [33]. The αmorphologies commonly encountered or that dominate in marine steels are the allotriomorphic and idiomorphic α . In this study they will collectively be referred to as α . The microstructure shown in Fig. 2(a) is air-cooled of medium carbon steel and the relatively rapid method of cooling, limited the α grain growth. The α then appears to form layers which followed the austenite grain boundary contours. The prior austenite grain boundaries are completely covered by the α allotriomorphs and the residual austenite has transformed into P upon reaching the temperature, 723 °C, of eutectoid reaction. The α phase is soft and ductile, while the$P$ is hard and brittle. P grows in colonies and each colony consists of a thin lamellar, alternating mixture of α (iron) and cementite, ϑ (iron carbide) or (α+$\Phi\epsilon_3$"). Fig. 2(b) shows a situation where the Fe - 0.4C steel is slowly cooled to room temperature, producing equiaxed grains. Several distinct$P$ colonies can be seen (dark etching). The α phase (light etching) is soft and ductile, while the P is hard and brittle. As the volume fraction of P increases the bulk strength increases and ductility decreases. If the carbon content of the steel is decreased, the volume fraction of P in the microstructure

Posted on Authorea 13 Apr 2020 — CC BY 4.0 — https://doi.org/10.22541/au.158679911.16268490 — This a preprint and has not been peer reviewed. Data may be preliminary.

will decrease while that of α increases as can be seen in Fig. 2(c). The morphology or shape of the α-Π phases therefore depends on the processing route discussed above and electrochemical composition. These two phases are of major interest in this study. Any other phase that might be present for the purposes of clarity is neglected.

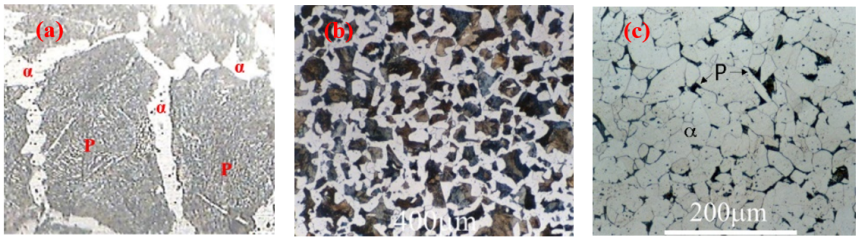

Fig. 2: Ferrite and pearlite morphologies: (a) ferrite in Fe-0.46 steel that forms layer tracing the austenite grain boundary contours [34], (b) equiaxed ferrite in a Fe-0.4C steel [33], (c) ferrite in low carbon steel [33] (α = ferrite, P = pearlite). The white etching is ferrite while the dark-etching is$P$.

The steels for this study are S355J2+N (J2N), S355G10+M (G10) and S355G8+M (G8) with compositions as given in Table 2. The composition of J2N was extracted from [35]. They are marine steels having low carbon contents with the microstructures consisting of very small volume fraction of P in a α matrix [36]. Fig. 3 shows the phase morphologies of the microstructure of the J2N.

Table 2: Chemical compositions and mechanical properties of test materials (see [36])

(CE = carbon equivalent)

Steel Grade	Notation	C	Mn	Ni	Si	Cu	Cr	Mo	CE	E %	YS (MPa)	UTS (MPa)
S355G10+M (TMCP)	G10	0.06	1.57	0.33	0.27	0.24	0.03	0.01	0.37	38	435	545
S355G8+M (TMCP)	G8	0.05	1.52	0.32	0.27	0.24	0.03	0.01	0.35	35	447	549
S355J2+N (NR)	J2N	0.17	1.54	0.04	0.04	0.08	0.02	0.10	0.57	20	385	531

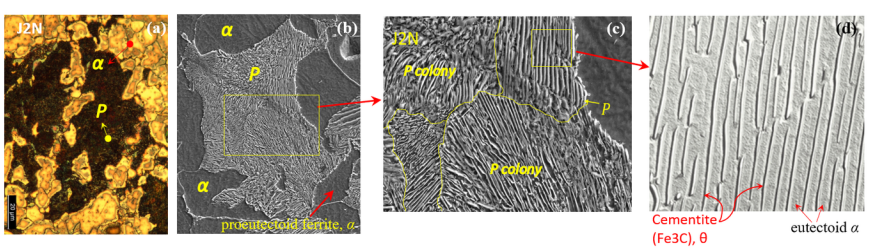

Fig. 3: Photomicrographs of α-Π steels - NR - S355J2+N

In Fig. 3(a), the optical micrograph shows that the microstructure is composed of P (dark etching) and the rest α (light etching). Microstructural examination of S355J2+N shows that, 80% of the microstructure is allotriomorphic α and others P , with traces of acicular or Widmanstätten α [37]. The P colonies in the J2N- steel are large, blocky and dense. This is a consequence of its chemical composition, heat-treatment and deformation or manufacturing method. Fig. 3(b) is the SEM micrograph of the microstructure. The blocky$P$ and the proeutectoid α , are noted accordingly. The proeutectoid α is the α phase that formed before the formation of P at the eutectoid temperature (723°C). Fig. 3(c) is the part denoted with a yellow box in Fig. 3(b) and the micrograph shows differently oriented Pcolonies as demarcated by the yellow lines. Fig. 3(d) shows what would have been the image of the part in the yellow box in Fig. 3(c) on a typical

Posted on Authorea 13 Apr 2020 — CC BY 4.0 — https://doi.org/10.22541/au.158679911.16268490 — This a preprint and has not been peer reviewed. Data may be preliminary.

transmission electron microscopy (TEM) micrograph. The structure that appears as parallel rods in that colony is the cementite (ϑ). Note that the ϑ plates are not generally continuous. The α that formed in between the ϑ rods are referred to as eutectoid α – because they are produced during the Pformation at the eutectoid temperature. Fig. 3(d), is extracted from Ref [33]. Fig. 4 shows the microstructures of G10, G8. These microstructures are found to be similar, but it is evident that they are distinct from that of J2N in Fig. 3. Fig. 4(a) is the optical image of G10 while Fig. 4 (b) is the SEM image. Similarly, Fig. 4(c) is the optical image of G8 while Fig. 4(d) is the SEM image. It is evident that the SEM image shows more details of the microconstituents. In both microstructures, the P nodules are very small compared to that of J2N and the volume fraction of the P is also less than that of J2N.

Fig. 5 shows the morphologies of the phases present in J2N in the rolling direction. The ferrite phase tends to have three forms – high relief (HR), low relief (LR) and ribbon like structure (HA) as shown in Fig. 5(a). Note that the low and high reliefα phase variants could not be distinguished under optical micrographs (see Fig. 3(a)). These features are important in analysing the work presented in this paper. For the purposes of description, letα_{HP} denotesα with high relief and $\alpha_{\Lambda P}$ is low relief while the ferrite ribbon is denoted α_{HA} . The yellow arrow shows the P , the blue arrow indicates theα_{HA} , the red arrow is theα_{HP} and the black arrow is the$\alpha_{\Lambda P}$. To the extent of information available to the authors, the α phase morphology observed in Fig. 5(a) is novel and has not been described in any literature elsewhere. Fig. 5(b to d) show the Energy-Dispersive X-ray (EDX) analyses of the chemical composition of the phases present in the J2N at locations 1 to 31 and the results are shown in Table 3.

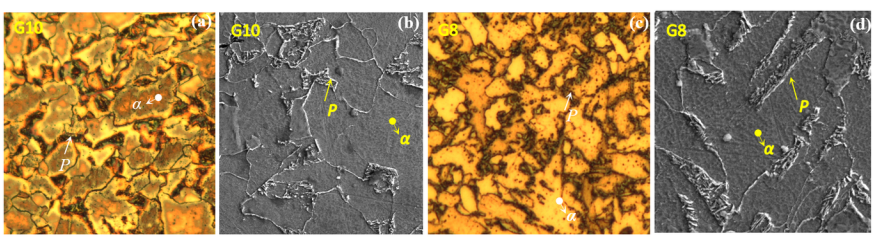

Fig. 4: Optical and SEM micrographs of α-Π $TMCP$ steels (a) TMCP - S355G10+M

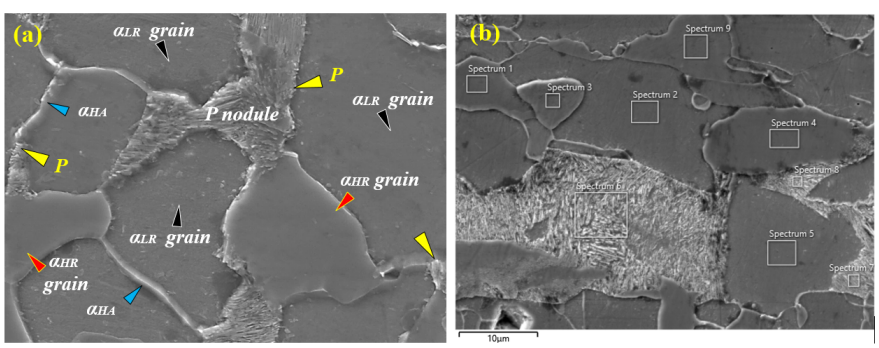

Posted on Authorea 13 Apr 2020 — CC BY 4.0 — https://doi.org/10.22541/au.158679911.16268490 — This a preprint and has not been peer reviewed. Data may be preliminary.

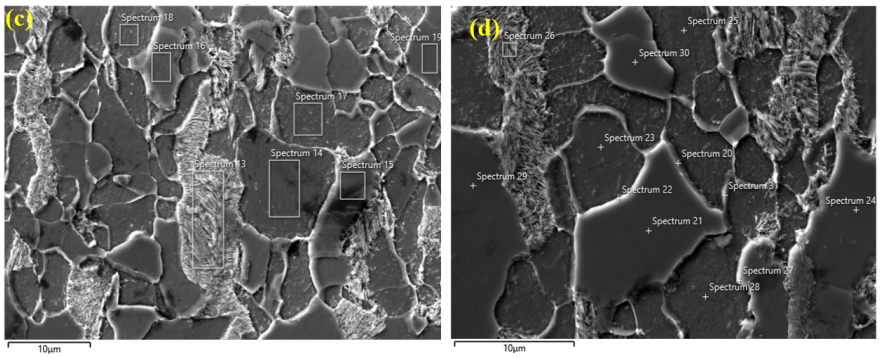

Fig. 5: EDX analysis of phase composition in S355J2+N steel

Table 3: EDX compositional average results of α and P phases in Fig. 5

(HR = high relief α, LR = low relief α, HA = α ribbon, EDX= Energy-dispersive X-ray analysis)

Spect. Label	C	Mn	Ni	Si	Cu	Cr	Mo	Al	Co	P	S	O	Fe
$\alpha_{\Lambda P}$ Average	5.50	1.41	0.09	0.37	0.02	0.02	0.01	0.12	0.41	0.02	0.01	0.10	91.79
α_{HP} Average	5.59	1.36	0.08	0.37	0.02	0.02	0.01	0.12	0.40	0.02	0.01	0.07	91.79
α_{HA} Average	9.86	1.41	0.09	0.46	0.04	0.02	0.01	0.17	0.39	0.03	0.01	0.45	88.12
P Average	9.33	1.50	0.08	0.40	0.06	0.02	0.01	0.11	0.38	0.02	0.02	1.38	86.59

The relative abundance of the alloying elements in the phases is in wt%. Note that the EDX composition simply shows the relative abundance of the alloying elements within an area in the phase and has no direct relationship with the steel overall composition shown in Table 2. In Fig. 5(b to d), locations 1, 3, 4, 16, 21, 30, etc., are areas of analyses on the α_{HP} , while 2, 5, 17, 25, 28, etc. are areas on the $\alpha_{\Lambda P}$. The light etching is the$P$, e.g. locations 6, 7, 8, 13, 26 etc. In Table 3, simple observation of the EDX results show that the alloying compositions of $\alpha_{\Lambda P}$ andα_{HP} are almost the same. But for theα_{HA} , all other alloy compositions are generally the same with that of $\alpha_{\Lambda P}$ andα_{HP} except that the amount of C, Si, Al and O are higher. The Fe content of α_{HA} and P are close, but lower than those of $\alpha_{\Lambda P}$ andα_{HP} . This tends to suggest thatα_{HA} is a ferrite phase with the highest concentration of alloying solutes. The P is found to have generally the same composition with the α_{HA} , but with higher oxygen content. An important note here is that the concentration of these solutes may weaken this phase, making it an easy path for FCG . General observed phase morphologies of J2N, G8 and G10 are shown in Fig. 6. Fig. 6 (a & b) are that of J2N obtained in the through thickness direction. The same basic microstructural features as presented in Fig. 5(a) were also observed in Fig. 6 (a & b). Fig. 6(c to i) present microstructural features in the $TMCP$ steels which are basically the same as that found in the J2N steel. For the $TMCP$, the P formed mainly between boundaries of the ferrite grains and with width that is relatively small. In the NR steel, P forms as dense and blocky phase in the αmatrix.

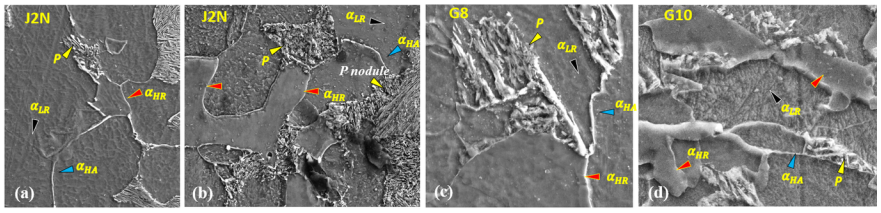

Posted on Authorea 13 Apr 2020 — CC BY 4.0 — https://doi.org/10.22541/au.158679911.16268490 — This a preprint and has not been peer reviewed. Data may be preliminary.

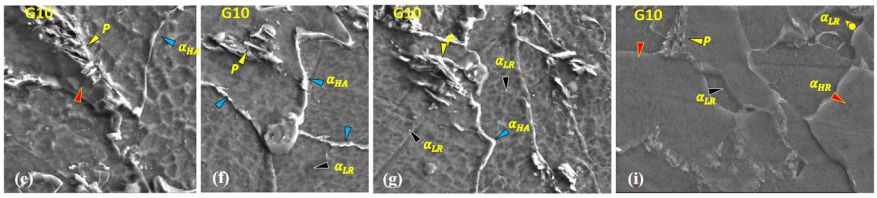

Fig. 6: Phase morphologies of J2N, G8 and G10 S355 steel subgrades showingα and P phases

FCGRs in NR and TMCP S355 steels in air

The formation of the microstructural phase morphologies described in Section 2 created different local microstructural properties. The presence of a hard phase (P) in a soft matrix (α) is expected to influence localFCG behaviour in steel [38]. The crack paths in these microstructures are also expected to vary. Steel microstructure influences fatigue crack propagation primarily by changing the mode of crack propagation. The mode can change from ductile striation to cleavage mode and the combination of the two modes increases crack propagation rates. There are many studies that claimed that microstructure has negligible effect at intermediate $FCGR$ s (Paris Region) [3][5][6][11][12] [13][14][18]. Some other study concluded that grain size affected sub-critical crack growth to the extent to which it affected fracture toughness,K_{Ic} and the onset of rapid fracture, and that grain size did not affect the FCG threshold,ΔK_{th} [4]. Zerbst [6] in his recent publication reported, I quote, '... *Perhaps the most astonishing observation is that the curve, in the Paris Region, is only slightly influenced by the microstructure of the material within whole material classes such as steels or aluminium alloys* .' In fact, it is commonly reported that microstructure has little or no influence in the Paris Region of the da/dN sigmoidal curve in air. Part of the presentation in this paper is to show what appears to be an influence of the $FCGR$ by microstructural phase morphologies in the Paris Region of the da/dN vs. ΔK curve.

In the recent studies, the authors evaluated the resistance of the NR and $TMCP$ steels given in Table 2 to FCG . The details of the experimental methods have been discussed in Refs [22][36][39]. The results of that experiment - for $FCGR$ tests in air are shown in Fig. 7. Shown also are the microstructures of the J2N and $TMCP$(G10 & G8) steels examined. In Fig. 7, it appears there is a demarcation between the $FCGR$ of NR and $TMCP$ in the Paris Region. The arbitrary line drawn as shown appears to be the separation line. The $FCGR$ in G8 and G10 steels are essentially the same and significantly lower than that of the J2N steels under the same experimental conditions. Generally, the $FCGR$ increased with increase in load level from 10kN to 12kN in J2N and also from 9kN to 10kN in $TMCP$. This is the expected trend in air, where increase in the fatigue load level increases the $FCGR$. We can also observe that the $FCGR$ in J2N for 10kN under 2Hz and 5Hz are essentially the same. This tends to confirm that frequency has no effect on the$FCGR$ of steel in air under the same loading conditions. To validate this finding, a comparative study of $FCGR$ in $NR$and $TMCP$ was carried out. The steel grade, chemical composition in wt% (approximated to two decimal places) and mechanical properties of the steels studied and compared with the data in this study are included in Table 4. The composition range for the steels in Table 4 is shown in Table 5. It is pertinent to note that BS4360 Grade 50D, Q345, RD480 and EH36 are equivalent to S355J2+N hot-rolled normalized steel. Q345 is common structural steel in China and used in the nuclear industry and petrochemical plants. Laurito studied $FCGR$ in intercritical-isothermally-quenched grain-modified steel designated as RD480. Though the chemical composition is comparable to other steels, the properties of the microstructure generated may differ significantly due to this heat treatment. Two microstructures of the same ABS grade EH36 steel produced by NR and $TMCP$ are presented. This steel is often used in shipbuilding. Comparing these two microstructures of the same alloy will clearly support this study. Table 6 lists all the studies and test conditions considered. All the steels are designed to be used in both onshore and offshore structures. They are fundamentally the same. The only difference perhaps is that the steels were produced under different proprietary methods by

Posted on Authorea 13 Apr 2020 — CC BY 4.0 — https://doi.org/10.22541/au.158679911.16268490 — This a preprint and has not been peer reviewed. Data may be preliminary.

different steel plants. All the tests were done under constant-amplitude sinewave, except Cheng [40] who performed his test under random waveform. The general range for temperature of the studies is about 27 °C to 0°C.

From the conclusions in the literatures [41][42][43][44][45][46][47], stress ratio (R) in the range 0.1- 0.85, frequency in the range 0.005Hz – 50Hz and waveforms appear to have little or no effect on the *FCGR* in theα-Π steels in air. Thus, the inferences here are within these limits.

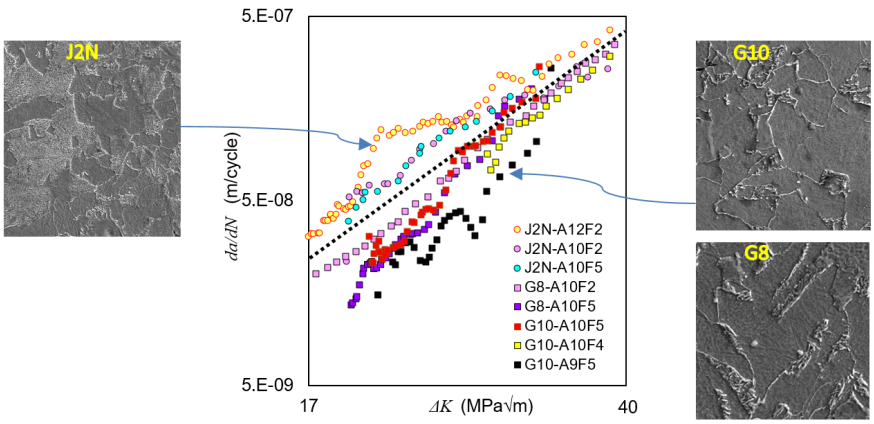

Fig. 7: Plot of FCGR in air for NR (J2N) and TMCP steel subgrades (G8 & G10)

Table 4: Chemical compositions of the ferritic steels for comparative study

Study	Steel Grade	C	Mn	Ni	Si	Cu	Cr	Mo	E%	YS (Mpa)
Scott [48]	BS4360-50D (*NR*)	0.18	1.38	-	0.37	-	-	-	32	370
Appleton [49]	BS4360-50D (*NR*)	0.13	1.22	-	0.32	-	-	-	32	368
Thorpe [50]	BS4360-50D (*NR*)	0.17	1.35	0.07	0.35	0.17	0.09	0.01	32	370
Musuva, [41]	BS4360-50D (*NR*)	0.18	1.40	0.10	0.36	0.16	0.11	0.02	30	386
Thompson [51]	BS4360-50D (*NR*)	0.15	1.38	0.10	0.41	0.02	0.11	0.01	30	386
Correia [52]	P355NL1 (*NR*)	0.13	1.38	0.12	0.35	0.14	0.03	0.00	-	418
Jesus [42]	EN 10025 S355 (*NR*)	0.10	0.64	0.10	0.15	0.38	0.08	0.01	22	419

Posted on Authorea 13 Apr 2020 — CC BY 4.0 — https://doi.org/10.22541/au.158679911.16268490 — This a preprint and has not been peer reviewed. Data may be preliminary.

Study	Steel Grade	C	Mn	Ni	Si	Cu	Cr	Mo	E%	YS (Mpa)
Adedipe [53]	S355J2+N (*NR*)	0.22	1.60	0.50	0.55	0.55	0.03	0.10	20	345
Xiong [54]	Q345 (NR)	0.15	1.54	-	0.34	-	-	-	26	370
Laurito [55]	RD480 (*IGM*)	0.09	1.17	0.01	0.05	0.01	0.02	0.01	32	459
Cheng [40]	EH36 (*NR*)	0.12	1.39	0.03	0.38	0.05	0.05	0.01	21	350
Callister [56]	K-50 (*TMCP*)	0.05	1.13	0.29	0.23	0.24	0.02	0.20	-	470
Tsay [57]	EH36 (*TMCP*)	0.13	1.32	0.03	0.31	-	0.03	-	21	420
Chapetti [58]	UFG – steel (*TMCP*)	0.15	1.80	-	0.20	-	-	-	14	696
PS (T)	S355G10+M (*TMCP*)	0.06	1.57	0.33	0.27	0.24	0.03	0.01	38	435
PS & Ali [59][60]	S355G8+M (*TMCP*)	0.05	1.52	0.32	0.27	0.24	0.03	0.01	35	447

Table 6: Experimental conditions for the studied steels in Table 4

Study by	**Steel grade**	**Wave form**	**Freq. (Hz)**	**R**	**%EL**	**YS (MPa)**
Scott [48]	BS4360-50D	s	1 - 10	0 - 0.85	32	370
Appleton [49]	BS4360-50D	s	-	-	32	368
Thorpe [50]	BS4360-50D	s	1 - 10	0.5	32	370
Musuva [41]	BS4360-50D	s	30	0.08, 0.5, 0.7	30	386
Thompson [51]	BS4360-50D	s	0.5	0.1	30	386
Correia [52]	P355NL1 (*NR*)	-	-	0.0	-	418
Jesus [42]	S355	s	[?] 20	0.25, 0.5 & 0.75	22	419
Adedipe [53]	S355J2+N	s	2	0.1	20	345
Xiong [54]	Q345	s	0.5	0.1 - 0.5	26	370
Laurito [55]	RD480	s	10	0.1	32	459
Cheng [40]	ABS grade EH36	r	10	0.1 & 0.5	21	350
Callister [56]	Kontroll-50 (*TMCP*)	s	0.5	0.6	-	470
Tsay [57]	EH36 (*TMCP*)	s	5	0.1	21	420
PS (T)	S355G10+M (*TMCP*)	s	4&5	0.1	38	435
PS & Ali [59][60]	S355G8+M (*TMCP*)	s	2&5	0.1	35	447

Posted on Authorea 13 Apr 2020 — CC BY 4.0 — https://doi.org/10.22541/au.158679911.16268490 — This a preprint and has not been peer reviewed. Data may be preliminary.

Study by	Steel grade	Wave form	Freq. (Hz)	R	%EL	YS (MPa)
s = sine, r = random, PS = present study	s = sine, r = random, PS = present study	s = sine, r = random, PS = present study	s = sine, r = random, PS = present study	s = sine, r = random, PS = present study	s = sine, r = random, PS = present study	s = sine, r = random, PS = present study

The marine steels have microstructures consisting essentially of small volume fraction of P in a α matrix. The morphology of the phases varied from banded to unbanded depending on the production process and sample thickness. The general microstructures of the steels in Table 4 are shown in Fig. 8. The grade of steel and the reference sources are also given. Fig. 8(a, b, c, d) are microstructures ofNR steels. The black etching is a banded P forming in the rolling direction and the light etching is the α . Fig. 8(e & f) are microstructures of the same NR steels, but taken from directions that are un-banded [37]. Fig. 8(g) is $TMCP$microstructure of the EH36 steel studied by Tsay [57]. The microstructure of $TMCP$ steels is greatly refined as compares to those of conventional or NR steels, resulting in a significant improvement in strength and toughness. Hardness was measured to be around $168HV_{0.1}$ with equiaxed grains of average size of 15μm, measured in the through-thickness direction.

Fig. 9 presents the plots of the $FCGR$ studies on the $NR$and $TMCP$ steels listed in Table 6, including the results of the present study (PS) in Fig. 7. For the test IDs in the PS , each sample is denoted with material type (e.g. J2N, G8 and G10), followed by the environmental air (A), the maximum load applied, P_{max}, on the sample (e.g. 10 kN), and the applied$f$ (e.g. F of 0.2, 0.3 and 0.5 Hz). The NR data points are denoted with circles in Fig. 9. The J2N data points in the PS are coloured yellow, the NR data points extracted from the literatures are green or black. The $TMCP$ data points are denoted with squares. The same trend observed in Fig. 7 is also seen in Fig. 9. It can be observed that in the Paris Region taken in the interval 20[?] ΔK[?]35, the$FCGR$ for the two microstructures separated into two domains, but with diffused inter-boundaries. The dash line is drawn arbitrarily to show possible demarcating line. Occupying upper half is the fatigue data points of NR steels and the lower half the $FCGR$ data points for the $TMCP$. In other words, the $FCGR$ in $NR$are generally higher than that of $TMCP$ in air.

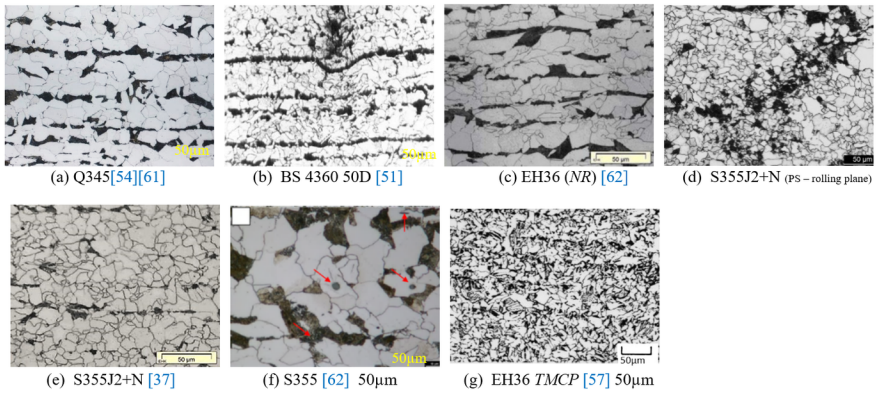

(a) Q345[54][61] (b) BS 4360 50D [51] (c) EH36 (*NR*) [62] (d) S355J2+N (PS – rolling plane)
(e) S355J2+N [37] (f) S355 [62] 50μm (g) EH36 *TMCP* [57] 50μm

Fig. 8**:** Typical microstructures of low alloy α- Π steels

One interesting note here is that even though the steels have similar micro-constituents, the $FCGR$ s are significantly apart, especially at low $SIFR$. Often, many researchers associate this variation in the Paris Region with material variability or crack closure (R-factor), but we could see that the margin of separation is very much significant – up to a factor of about 4 from the two extremes. An important observation also is that the$FCGR$ of the two microstructural variants (NR &$TMCP$) of the EH36 steel studied by Cheng [40] (NR) and Tsay [57] ($TMCP$) under similar experimental conditions are different. The $FCGR$ data of the

Posted on Authorea 13 Apr 2020 — CC BY 4.0 — https://doi.org/10.22541/au.158679911.16268490 — This a preprint and has not been peer reviewed. Data may be preliminary.

EH36 (*NR*) denoted with black circle in Fig. 9 partitioned into the *NR* domain while that of EH36 (*TMCP*) separated into the *TMCP* domain as shown by the black square. Note that within this region the effect of crack closure is insignificant or negligible. In general, Fig. 9 tends to suggest that microstructure affected the *FCGR* in air.

Microstructure and FCG path in air

Post-failure examination of the fatigued surfaces in air revealed features shown in Fig. 10. The fractographs Fig. 10(a & b) were obtained from the *NR* steel (J2N), while that of Fig. 10(c & d) were obtained by Adedipe [63] for the same steel grade. Fig. 10(e) is the fractograph obtained in air for the *TMCP* steel. The part in a red box in Fig. 10(e) was magnified as shown in Fig. 10(f) and the area in the red box in Fig. 10(g) was magnified to that shown in Fig. 10(h). From all the fractographs, it is very obvious that the failure in air had occurred by ductile striation mechanism (*DSM*) with secondary crackings (*SC*) as shown by the arrows. Few *SC* in the normalised steel, J2N and more *SC* in the *TMCP* were observed. The occurrence of the *SC* increased with increase in*SIFR* . Striations were seen even inside the secondary cracks as can be seen in Fig. 10(f & h). This shows that the groove was made by a moving crack front and not due to brittle cracking or cleavage. The*DSM* as seen in the fractograph is typical of the failure mechanism in the Paris Region for low carbon steel. These fractographs do not give significant clue to the observed difference in the*FCGR* in Fig. 7 and Fig. 9. An altervative approach is to examine the crack path and the features influencing crack growth in the materials.

To understand the disparity in the *FCGR* between *NR* and the*TMCP* steels as presented in Fig. 7 and Fig. 9, a crack path metallography was carried out and the result is presented in Fig. 11 for the *TMCP* steel, G8. Fig. 11(a) shows the general crack paths seen in the *TMCP* steels in air for 10kN, 5Hz, stress ratio of 0.1, under sinewave. The yellow double line arrow in the figures shows the direction of the applied fatigue load. The long crack path was obtained for [?]K of about 18.52 to 34.25 MPa[?]m, i.e. fully in the Paris Region. It is very clear that the crack path is non-planar and complex. The traces of the crack path are given in Fig. 11(b). The crack path has extensive high degree of large angle crack diversions, multiple bifurcations and crumb formations as noted clearly in Fig. 11(b).

Posted on Authorea 13 Apr 2020 — CC BY 4.0 — https://doi.org/10.22541/au.158679911.16268490 — This a preprint and has not been peer reviewed. Data may be preliminary.

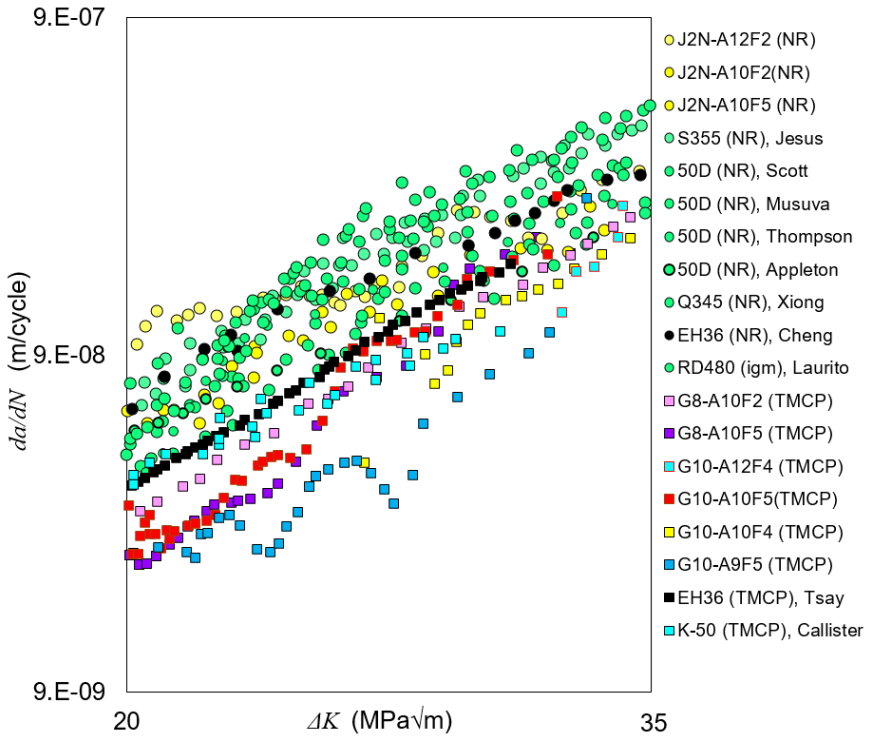

Fig. 9**:** The FCGR in NR and TMCP in air in the Paris Region with demarcation line

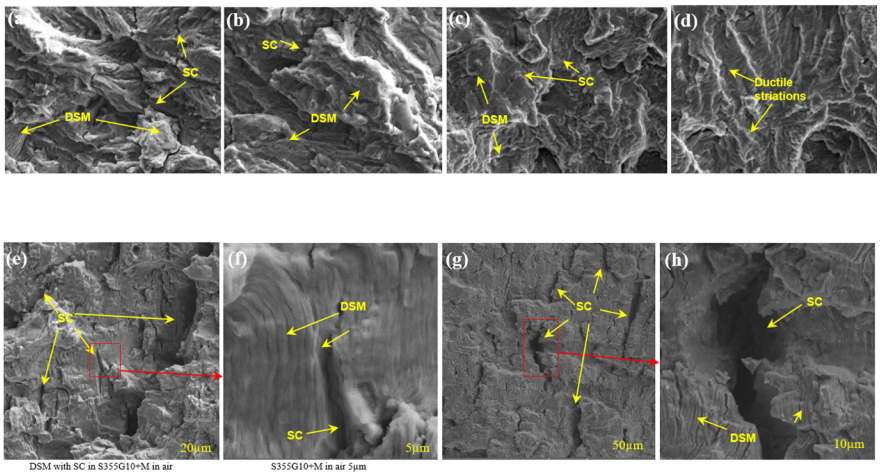

Fig. 10: Fractographs of fatigued surfaces (a-d) for J2N, (e-h) for the G10 in air

(Ductile striation mechanism (DSM) with secondary crack (SC))

The metal crumbs were formed in between branched and re-joined crack fronts. It can also be observed that several small metal crumbs were formed as the crack propagated in air and the occurrence increased with increase in [?]K . In other words, the tendency for crack branching and re-joining tends to increase with increase in the driving force for crack propagation. The length of the branched crack is considerably long,

Posted on Authorea 13 Apr 2020 — CC BY 4.0 — https://doi.org/10.22541/au.158679911.16268490 — This a preprint and has not been peer reviewed. Data may be preliminary.

and the extent of bifurcation angle is substantially large. Fig. 11(c) is the magnification of the locations 1 to 8 marked with the yellow boxes. It was observed that the branched crack fronts generally followed the thin ribbon a_{HA} phase as shown in the magnified locations. This tends to suggest thata_{HA} is the path of least resistance. An important feature of the crack growth is that generally the tip of the propagating crack was always sharp as can be seen from the tip of the branched crack front as shown in the magnified micrographs in Fig. 11(c).

Hosted file

`image15.emf` available at https://authorea.com/users/311001/articles/441756-the-influence-of-microstructure-on-the-fatigue-crack-growth-rate-in-ferrite-pearlite-steels-in-the-paris-region

Fig. 11**:** Crack path (a) in *TMCP* steels in air: G8, 10kN, 5Hz, sinewave at a scale of 20 µm, crack length between about 20.33 mm (18.52 MPa[?]m) to 30.09 mm (34.25 MPa[?]m), (b) schematic of the crack path, (c) magnification of the crack front

(direction: from right to left)

The crack tip maintained its sharpness throughout the Paris Region in the range 18.52 to 34.25 MPa[?]m. For the fact thata_{HA} could influence crack front diversion in the Paris Region is very important in the design of fatigue resistant steel. The fractographs of fatigued surfaces as shown in Fig. 10 can only show mechanism of the growth but cannot show these phenomena found in Fig. 11 specially the formation of the metal crumbs, which has not been reported in any literature. Due to many branched and arrested cracks, it is expected that the fractography of the fractured surface for this sample will likely show many occurrences of *SC* s. This is evident in Fig. 10(e & g) where many secondary cracks are present.

Fig. 12(a) shows the crack path observed in *NR* steel in this study. Relative to the crack morphology in the *TMCP* (see Fig. 11(a)), a low-angle crack diversion and low-angle, short-length branching were seen. The red arrows show the low-angle crack diversion, the black arrows the low angle crack branching and the white arrows show some metal bits or crumbs. Fig. 12(b) is the schematic of the crack path showing clearly the enumerated features. This *NR* crack path is clearly different from that of the *TMCP* (Fig. 11(b)) and it is a function of the microstructural features. In comparison with the crack growth path in J2N, the crack path in the *TMCP* is more complex with extensive high angle crack diversion and crack branching. The lengths of the branched cracks are considerably longer than that of J2N. There was also severe formation of relatively large metal crumbs in air in *TMCP* than in J2N. Several small metal crumbs were also seen as the [?]K increased. The crack-tip diversion, branching and creation of metal crumbs can reduce the effective stress at the local crack tips resulting in retardation of the *FCGR* . Fundamentally, the degree of crack tip stress shielding will vary with the angle of crack-tip diversion and the nature of metal crumbs created. The metal bit will be effective in retarding the crack growth if it re-orients and causes mismatch or wedging action. The tendency to re-orient may increase if the crumbs are smaller in rough-round shape rather than in plate-elongated form. These two natures of metal crumbs will be a function of the steel microstructure

Hosted file

`image16.emf` available at https://authorea.com/users/311001/articles/441756-the-influence-of-microstructure-on-the-fatigue-crack-growth-rate-in-ferrite-pearlite-steels-in-the-paris-region

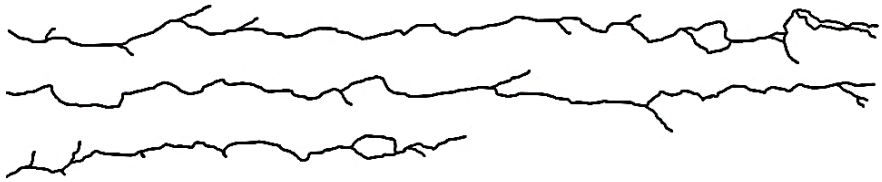

Fig. 12: Fatigue crack path (a) in J2N steel in air (10kN, 5Hz at a scale of 20 µm) (b) schematic of the crack

Posted on Authorea 13 Apr 2020 — CC BY 4.0 — https://doi.org/10.22541/au.158679911.16268490 — This a preprint and has not been peer reviewed. Data may be preliminary.

path

(direction: from right to left)

Fig. 13 shows the *FCGR* s in two samples of the *NR* (the circle data) and three samples of the *TMCP* (the square data) steels. As noted, the tests were performed in air under similar test conditions at 10kN and 2Hz, 5Hz for the three materials - J2N, G8 and G10. Note that the microstructures of G8 and G10 are generally the same (see Fig. 4). The *FCGR* s at 10kN, 2Hz (J2N-A10F2) and that of 10kN, 5Hz (J2N-A10F5) are generally the same, though that of J2N-A10F2 is slightly higher. This may be because the maximum fatigue loading, P_{max} can be fully delivered during test at reduced frequency. Generally, these tests show that the effect of frequency on*FCGR* in air is negligible within the same steel subgrade. An important feature of the crack growth is that generally the tips of the propagating cracks in the *TMCP* steel are always sharp throughout the Paris Region (see Fig. 11(c)). High angle crack bifurcation and diversion are generally absent, and the formation of metal crumbs are few in the *NR* steel. This explains the reason for the higher*FCGR* in the *NR* as compared with the *TMCP* steel. This implies that, the longer the branched arms; the more the diversions and branching angles; the more the crack growth is retarded due to re-distribution and reduction of the driving force at the main crack tip. Where the three phenomena are few, one would expect a high*FCGR* .

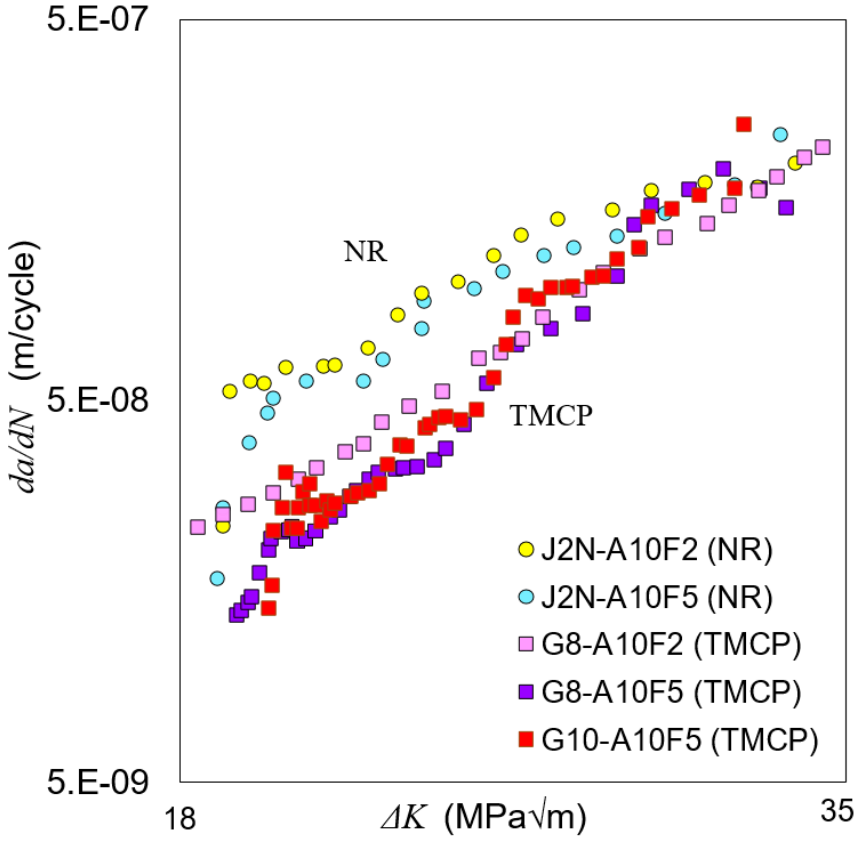

Fig. 13: *FCG* curves in NR and TMCP steels

Posted on Authorea 13 Apr 2020 — CC BY 4.0 — https://doi.org/10.22541/au.158679911.16268490 — This a preprint and has not been peer reviewed. Data may be preliminary.

Assessment of FCGR path and mechanism in air

From the previous discussions, it is obvious that the material microstructure influenced the $FCGR$by crack path diversion, branching and formation of metal crumbs in-between branched and re-joined crack fronts. High FCG retardation was obtained when large angle diversion, large angle branching and change in the orientation of metal crumbs occurred. Some of the distinct micrographs showing phases and morphologies influencing the $FCGR$ are presented in Fig. 14 for the NR steel and Fig. 15 for the $TMCP$steel. The phases where obtained by scanning along the entire length of the fatigue crack from the initiation point to point of test stoppage.

Hosted file

`image19.emf` available at https://authorea.com/users/311001/articles/441756-the-influence-of-microstructure-on-the-fatigue-crack-growth-rate-in-ferrite-pearlite-steels-in-the-paris-region

Fig. 14: Effect of microstructure on FCGR in NR steel in air, for 10kN, 5Hz

Fig. 14(a, b & c) shows instances of the propagation of the crack that initiated from the C(T) specimen notch of length 20.50 mm. In existing theory, a long crack is regarded as a fully developed crack with attendant plastic-induced crack closure effect and of length usually greater than 0.5 mm [18], the plastic zone is larger than one-fiftieth of the crack length ($r > 1/50a$) and the rate of crack propagation is described by the Paris law. At a length of 20.50 mm, the crack shown in Fig. 14 is a very long one. The dotted yellow line shows the boundaries of the grains. The encircled spaces by the yellow dotted lines are the ferrite grains while the red dotted lines, where used, encircled the pearlite nodules. The white solid line shows the movement of the fatigue crack through the microstructural phases. The dots in Fig. 14(a) showed crack fronts that stopped growing while the arrow indicates the mean active crack front. In Fig. 14(a, b & c), the crack appears to have initiated from and then propagated along what appears as the grain boundaries or 'intergranularly'. A closer observation shows that the crack propagated through the thin ribbon of the high alloy ferrite phase,α_{HA} , that surrounds the$\alpha_{\Lambda P}$ grain surfaces. This mode therefore is properly referred here as *quasi-intergranular* cracking mode. At the point marked X in Fig. 14(a), the thin ferrite phase ribbons, shown by the blue triangular arrows is not favourably aligned to the crack front – i.e., they are aligned at a very high angle, towards the vertical, to the crack front. In this case, the crack will have to advance transgranularly through the grain $\alpha_{\Lambda P}$ in front of it. In Fig. 14(b), the α_{HA} is aligned favourably or lies at low angle to the crack front, hence, the crack advanced following this ferrite ribbon. Similar situation is seen in Fig. 14(c), however, it appears that the grain of$\alpha_{\Lambda P}$ in front of the advancing crack front resisted transgranular propagation of the crack in the direction 1 and this caused the nucleation of another crack front that attempted to follow the α_{HA} (shown by the blue arrow) in direction 2. This resulted to crack bifurcation and tends to suggest that the α_{HA} or the$\alpha_{\Lambda P}/\alpha_{HP}$ boundary is the preferred path for the crack growth, especially when the boundary is lying at low angle to the crack growth plane. Note that in Fig. 14(a, b & c), theα phase dominated the local area with no P phase.

As the [?]K increased and the crack moved into local areas of mixedα and P phases as in Fig. 14(d to k). This region is dominated by the $\alpha_{\Lambda P}$ phase and some few Pcolonies. The α_{HP} is almost absent in this region. It appears that the P is equally likely to cause crack-tip diversion and crack branching, but a closer examination showed that these phenomena had been influenced to some extent by theα_{HA} which appears to serve as the origin or starting phsase for the P formation. Fig. 14(d) shows intragranular crack growth and bifurcations, however, one could see that some of the crack tip followed α_{HA} phase. Fig. 14(e) shows the formation of metal crumb and this microstructural region is also dominated by the $\alpha_{\Lambda P}$. Fig. 14(f to j) show crack branching in the P phase. The tendency for crack branching in the P may be attributed to the orientation of the$P$ -colonies and α_{HA} boundaries. In the first case, this tendency may be because the pearlite has two alternating phases – ferrite, α (iron, Fe) and cementite,ϑ (Fe_3C) [64][65] with different physical and chemical properties. Daeubler [66] studied the influence of microstructure on the surface FCG behaviour of pearlitic steels and presented a classical case where the$P$ -colony orientation influenced the

Posted on Authorea 13 Apr 2020 — CC BY 4.0 — https://doi.org/10.22541/au.158679911.16268490 — This a preprint and has not been peer reviewed. Data may be preliminary.

crack growth, especially when the lamellae are favourably oriented to the load axis. In the present study (PS), it was observed that$\alpha_{\Lambda P}/\alpha_{HA}$ or andα_{HA}/Π boundaries are preferred paths ofFCG . The blue arrow in Fig. 14(i) shows a branched crack that followed the α_{HA} and the black arrow in Fig. 14(j) shows what appears to be a branched crack front following$\alpha_{\Lambda P}/\Pi$ boundary. Fig. 14(k) shows another metal crumb that formed in the vicinity of mainly $\alpha_{HP}$and $\alpha_{\Lambda P}$ phases. It appears that the formation of the metal crumb occurs in the α_{HP} and$\alpha_{\Lambda P}$ phase fields as shown in Fig. 14(e & k).

Fig. 15 shows crack path for G8 test in air, under 10kN, 5Hz stress ratio of 0.1 and sinewave. The crack length measured about 10 mm obtained under [?]K of about 18.50 to 34.25 MPa[?]m. The number of high angle diversion and crack branching is by far more in the$TMCP$ steel as compared with low angle crack-tip diversion and crack branching that was consistently found in NR (see Fig. 14). Measurements of the angle of crack branching in NR steel show that they are generally below 45°. The only time high angle diversion was found to be a little above 45° inNR steel is when the crack is avoiding$\alpha_{\Lambda P}$ phase or following the α_{HA} or α/Π boundaries that is favourably oriented in its path. The α is shown in Fig. 15 by the blue triangular arrow. The space enclosed by the red dotted line is the P while the yellow dotted line is the α . Multiple formations of metal crumbs are also shown. These micrographs show that the $\alpha_{\Lambda P}$ dominated the microstructure with extensive formation of the α_{HA} . Many of theα_{HA} appear as sub-grain phases inside the $\alpha_{\Lambda P}$ grains. The presence of α_{HP} is very small and the$P$ -nodules are very small also - even some nodules are purely single colonies. The crack path in the $TMCP$ steel is completely non-planar and more complex than that of the NR steel.

Hosted file

`image20.emf` available at https://authorea.com/users/311001/articles/441756-the-influence-of-microstructure-on-the-fatigue-crack-growth-rate-in-ferrite-pearlite-steels-in-the-paris-region

Fig. 15: Fatigue crack growth in TMCP, G8, 10kN, 5Hz in air

It was observed that the crack-tip diversion and branching in Fig. 15 were caused by the crack tip following path of least resistance created mainly by the α_{HA} or the$\alpha_{\Lambda P}/\alpha_{HP}$ boundaries - but mostly by the α_{HA} ribbons. The crack bifurcation is quite extensive with long arms as can be seen in Fig. 15(a to e) and the diversion of the main active crack front as shown in Fig. 15(f) was measured to be about 43$^{?}$ to the horizontal plane. The branched arms are measured to be in the range 38$^{?}$ - 46$^{?}$. It is interesting to see that the path of least resistant caused many of the branched arms to deviate almost at an angle within this range. This simply implies that both tensile and shear stresses continuously acted on the crack as it propagated in the$TMCP$, even in the Paris Region! The metal crumbs as noted in Fig. 15 are by far more in the $TMCP$ than the NR steel. It was observed also that the α_{HA} does not only have the potency to divert and branch out crack front, it can as well facilitate re-joining of branched crack fronts into one main crack front resulting to the crumb formation. This crumb is found to be a tore-off of the steel grain or block of grains. In other words, the fatigue crack front in α-Π steel appears not to have a horizontal crack-tip edge, but rather series of fluctuating wavelike crack front, whose nature depends on the steel grains and the phases surrounding the grain surfaces. It is important to note that this metal crumb along the crack path has not been reported elsewhere in the literatures or considered in any theoretical formation or treatment. The P- colonies in theNR steel are large, blocky and dense. In the $TMCP$ steels, the P appears to grow in two forms – small-blocky colony and a thin, elongated or needle-like morphology colony along what may be described as the α grain boundaries as shown, in some cases, by the space enclosed with the red dotted line in Fig. 15. The effect of thermomechanical control rolling process appears to be the disruption of the P banding and blocky morphology into randomly distributed thin P needles. From the observation, it appears that the interface between the α and P is an additional effective preferable path for the crack growth if the P -nodule is elongated and aligns favourably to the crack front. In Fig. 15, the branched cracks did not just move about linearly but tends to trace theα_{HA} phase. This suggests that the energy needed to propagate through the α_{HA} is much less than that for traversing the $\alpha_{\Lambda P}$ grain. The influence of the phase morphology persisted to a length of 9 mm and at 32 MPa[?]m.

Posted on Authorea 13 Apr 2020 — CC BY 4.0 — https://doi.org/10.22541/au.158679911.16268490 — This a preprint and has not been peer reviewed. Data may be preliminary.

The existing theory says that the crack path in the Stage II of the da/dN vs. [?]K sigmoidal curve is generally across the grains - transgranular [17] and the material microstructure has little or negligible effect in this region [3][5][6][18]. It can be seen that the crack path in the NR in Fig. 14 and that of $TMCP$ in Fig. 15 are not the same. The extensive crack diversion, bifurcation and metal crumbs formation retarded the $FCGR$ and explains why the $FCGR$ in the $TMCP$ is lower than that of the NR in Fig. 13. This finding appears to show that microstructure has a strong influence on the rate at which fatigue crack grows in α-Π steel in air. This assertion is contrary to the existing theory that microstructure of a steel has little or negligible effect on the $FCGR$ in air. Again, both transgranular and intergranular modes of propagation were observed in air. What appears as the intergranular cracking mode predominated in the $TMCP$ steel. However, what appears as an intergranular mode is actually the growth of the crack through the thin layer of α_{HA} in between the grains of $\alpha_{\Lambda P}$ or the P . Hence this mode is identified here as the *quasi-intergranular* mode. The morphology and chemistry of the microstructural phases and load level appear to determine which mode the crack growth will adopt.

Another factor is that the angle the crack front makes with the phases ahead of it tends to determine if it would propagate in transgranular or *quasi-intergranular* mode. However, in Fig. 10(f) ductile striations were found inside the secondary crack – which actually appears as a branched crack when viewd from the crack line. This clearly shows that the mode is not strictly intergranular, but the crack moved in the α_{HA} phase ribbon immediately adjacent to the $\alpha_{\Lambda P}$ or the P interface, justifying the use of word - *quasi-intergranular* . In general, $TMCP$ steel is more resistant to crack propagation than NR steel of the same steel grade. This is made possible by its refined microstructure that branched (with long arms) and diverted the crack front at large angles as compared to the small angle path diversion found in the NR steel. It must be noted that the ability of the α_{HA} to deviate crack front appears to lie in its alloying composition relative to the surrounding phases. The α_{HA} clearly has more of carbon, silicon and oxygen contents than other phases (see Table 3). The increase in the amount of these elements might have embrittled the phase, making it the least resistant path.

FCGRs in NR and TMCP S355 steels in seawater

A similar study described in Section 3 was carried out in SW . The authors assessed the FCG resistance of J2N, G8 and G10 given in Table 2 in SW . The details of the experimental procedures have been discussed in Refs [22][36][67]. The experimental results are shown in Fig. 16. Three corrosion fatigue crack growth rate ($CFCGR$) curves, obtained at 12kN, 9kN and under 0.3Hz, for the J2N studied by Adedipe [53] (abbrev. 'Ade') were plotted from the data extracted from a vs. N curves given in Ref [53]. In the present study, one test on the J2N was performed at 9kN, 0.3Hz, R = 0.1 to validate the results obtained in the Adedipe's study. Mehmanparast [59] studied $CFCG$ in G8 under similar loading conditions and at three different test locations noted as (A3, A4), (B3, B4) and C3. In identifying the experimental samples, the prefix gives the steel subgrade – J2N, G8, G10, followed by S (S = sinewave), P_{max} (maximum load), F (frequency, followed by the frequency value) and the last is the test centre for the Mehmanparast [59] study. All the tests were performed in SW and under sinewave.

Posted on Authorea 13 Apr 2020 — CC BY 4.0 — https://doi.org/10.22541/au.158679911.16268490 — This a preprint and has not been peer reviewed. Data may be preliminary.

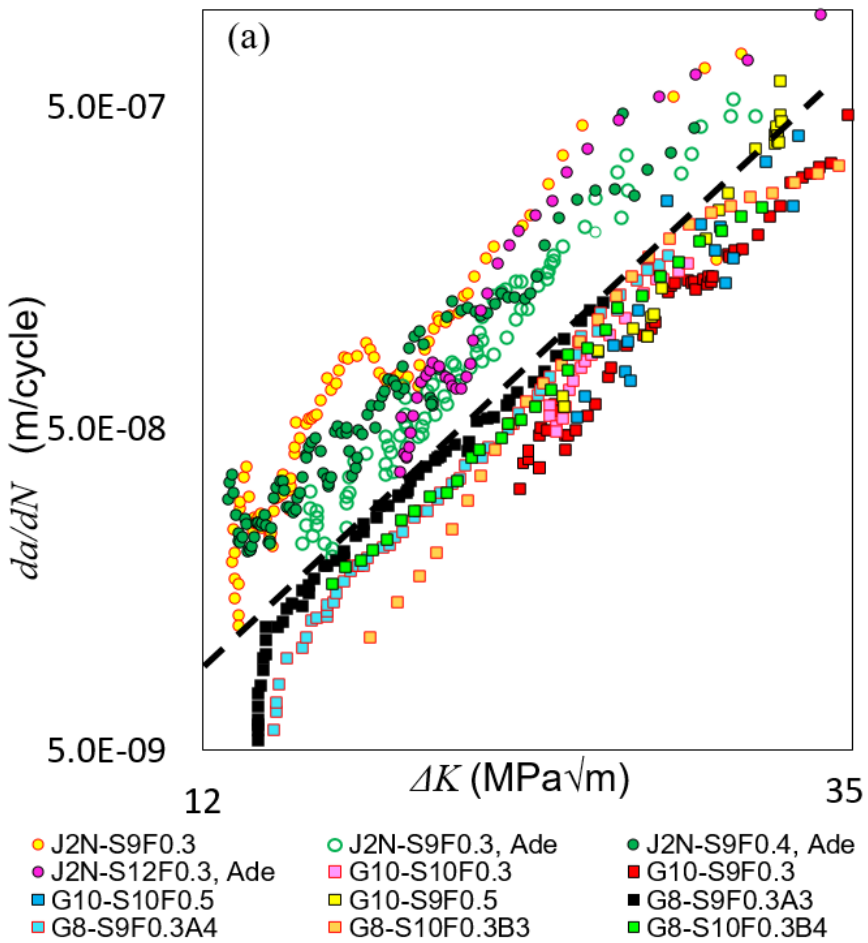

Posted on Authorea 13 Apr 2020 — CC BY 4.0 — https://doi.org/10.22541/au.158679911.16268490 — This a preprint and has not been peer reviewed. Data may be preliminary.

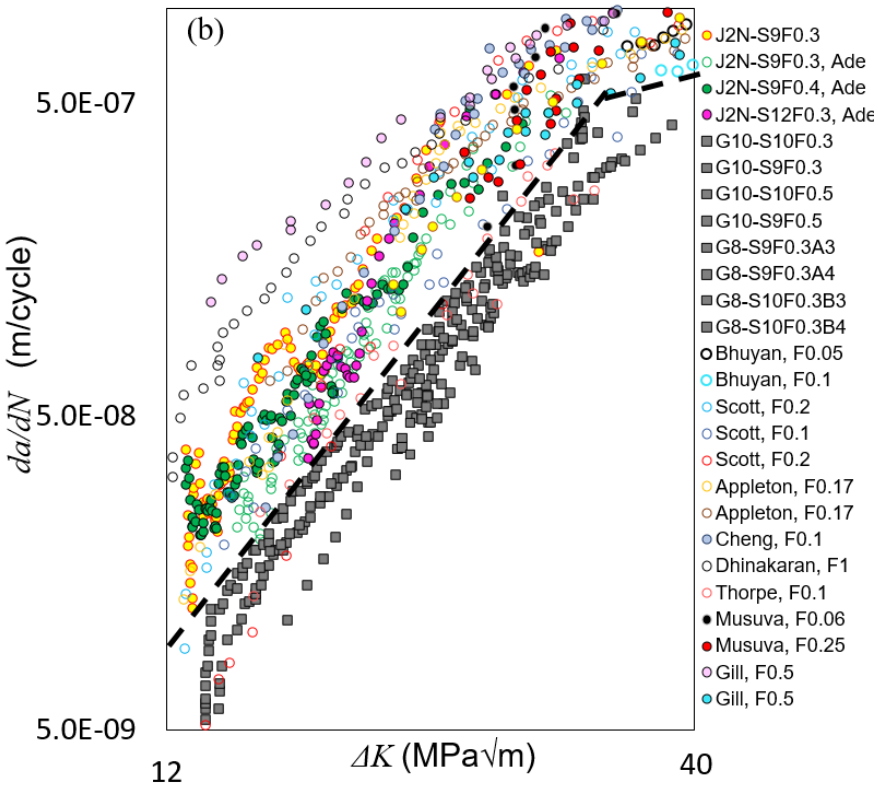

Fig. 16: Plot of FCGR in *SW* (a) NR and TMCP steels in the present study (b) CFCGR curves of *α-Π* steels reported in the literatures

Fig. 16(a) appears to show the partitioning of the *FCGR* s of*NR* and *TMCP* steels in *SW* into two domains as demarcated by the arbitrary dash line. The *CFCGR* s for the*NR* steel occupy the upper region of the dash line and that of the*TMCP* the lower region. The result of the *NR* steel tends to show that decreasing the fatigue load level has more accelerating effect than increasing the load as shown by the 9kN and 12kN under 0.3Hz. Selected results for the G8 steel study by Mehmanparast [59] show that increasing the fatigue load level to 10kN at 0.3Hz did not necessarily increased the *CFCGR* above that of 9kN. In fact, below about 18.50 MPa[?]m, the *CFCGR* of the 10kN decreased below that of 9kN. For the G10 steels, two load levels – 9kN, 10kN and two frequencies 0.3Hz, 0.5Hz were used. At about 20 MPa[?]m and above, there is no obvious difference in the *CFCGR* for the test conditions. In general, the *CFCGR* s of G10 for all the test conditions were slightly lower than that of G8 and the *CFCGR* s of all the*TMCP* subgrades were lower than that of the J2N steel. In fact, the dash line shows possibly the line of demarcation, though diffused, between the *CFCGR* s of the *NR* and *TMCP* S355 steel subgrades.

In a similar way to air study, the trend found in Fig. 16(a) is validated by carrying out a comparative study of *CFCGR* s between *NR* and *TMCP* *α-Π*steels reported in the literature. The steel grades and mechanical properties of the steels compared with the *CFCGR* data in the present study are shown in Table 7. It must be mentioned that there are limited studies on the corrosion fatigue of marine steels under the conditions listed in Table 7. Fig. 16(b) presents the *CFCGR*studies on the steels listed in Table 7. A large separation in the*CFGCR* s between the *NR* and *TMCP* steel is once again observed. It can be observed from Table 7 and Fig. 16(b) that*CFCGR* s of even some studies carried out at low stress ratios, such as 0.08 by Musuva [41] where higher than those of the*TMCP* in Fig. 16(b). It is often reported in the literatures that plasticity-induced, roughness-induced and oxide-induced crack closure can cause crack growth retardation. It is pertinent to note that during fatigue, the surface asperities or roughness is caused by the ductile stretching

Posted on Authorea 13 Apr 2020 — CC BY 4.0 — https://doi.org/10.22541/au.158679911.16268490 — This a preprint and has not been peer reviewed. Data may be preliminary.

or tearing of the fractured surface. These features are areas of high energy and would corrode very fast if in contact with corrosive environment, leaving a smooth surface or deep contour in the case of plastically deformed regions. Hence, they would not contribute significantly to crack retardation. The only factor that may likely cause retardation is oxide-induced crack closure and the extent may depend on the flow rate of the corroding medium and the stress ratio.

Table 7: Experimental conditions for the CFCGR data used in this study

Study by	**Steel grade**
Bhuyan	CSA G40.21M 350 WT
Scott	BS4360-50D
Appleton	BS4360-50D
Cheng	ABS grade EH36
Dhinakaran	C-Mn steel
Thorpe	BS4360-50D
Adedipe	S355J+2N
Musuva	BS4360-50D
Gill	HSLA (MF-80)
PS	S355G8+M
PS	S355G10+M
	S355J+2N
s = sine, t = triangular, p-s = positive sawtooth, n-s = negative sawtooth, SW = seawater	s = sine, t = triangular, p-s =

Microstructure and FCG path in seawater under sinewave

A metallographic study was carried out to assess the cause of the disparity in the *FCGR* s between *NR* and *TMCP* as observed in Fig. 16. The fractographs for the *NR* and *TMCP*steels in *SW* are shown in Fig. 17. Fig. 17(a) is the fractograph obtained in the present study for J2N and Fig. 17(b) is for the same steel obtained by Adedipe [63]. Fig. 17(c) is the corrosion-fatigued surface of the G10 obtained at about 20MPa[?]m and Fig. 17(d) is the common feature of the corrosion-fatigued surface of the same material above about 23 MPa[?]m. Generally, cleavage cracking was not observed and the failure mode remains by ductile striation which is typical of the failure mechanism in the Paris Region for low carbon steel.The striations in *SW* simply appeared to be washed out by the corrosion process and the surfaces were covered by the corrosion products. This washing out progressed with time as can be seen from (c) to (d) in Fig. 17. The secondary cracks in the *TMCP* steel were larger than that of *NR* and the corrosion products appear to collect into these secondary cracks over time as seen in Fig. 17(d).

The collection of the corrosion products into the cracks has the potential of reducing the crack driving force, hence, the rate at which the crack is moving. However, the flow of test environment and pumping of the*SW* in and out of the crack tip as a result of the cyclic action – especially under sinewave, has the capacity of removing corrosion products at the crack tip. Hence, oxide-induced retardation effect may be minimal. Moreover, crack closure phenomenon is little or negligible in the Paris Region. Since there was no cleavage cracking in the J2N, retardation due to the corrosion product or the oxide-induced crack closure is

Posted on Authorea 13 Apr 2020 — CC BY 4.0 — https://doi.org/10.22541/au.158679911.16268490 — This a preprint and has not been peer reviewed. Data may be preliminary.

not sufficient to account for the large difference in $CFCGR$ s in Fig. 16. An altervative approach again is to examine the crack path and the microstructural features influencing crack growth in the medium. Fig. 18(a) shows crack path in the G10 material in SW . Fig. 18(b) is a schematic of Fig. 18(a). The direction of all the crack growth is from left to right and the direction of applied fatigue force is as given by the yellow double-edge arrow. The crack path was observed for the G10 under sinewave, 9kN and 0.2Hz between the [?]K of 19.34 and 30.19 MPa[?]m. The same phenomena of high angle crack path diversion, multiple crack branching and metal crumbs phenomena characteristic of this $TMCP$ steel in air were also observed in SW (as shown in Fig. 18(b)). But, the number of the branched crack fronts is somewhat less and the extension or length of the branched arm is short compared to that of air. It then appears that the corrosion process had limited the length of the arm of the branched crack through a blunting process. Metal crumbs were also observed, but the extent is small compared to the air test.

Another feature that can be seen is the corrosion attack of the separated surfaces which resulted to widening of the fatigued surfaces as compared with the test in air (see Fig. 11). This widening process may be due to elimination of the small metal crumbs, plastically deformed wake and the '$microplastic$ -zone by the corrosion process. The$microplastic\ zone$ as used, refers to the closest area(s) to the crack tip that experienced the greatest lattice distortion, stress intensity or plastic deformation as a result of the amplified cyclic force at the crack tip as it opens and closes. These are areas of high lattice energy and are expected to be the points of greatest corrosion rate. Another observation of high importance is that the crack tips of both the main and branched crack fronts from number 1 to 5 are largely sharp as shown by the magnified micrographs of Fig. 18(c). However, the areas immediately behind the crack tips are widened by the corrosion process as compared with that of the air. It was observed also that the sharpness of the crack tip decreased gradually with increase in the [?]K . It may be that at high [?]K , the crack-tip was sufficiently open to allow some degree of blunting by the corrosion process. This generally suggests that the crack tip under 9kN, 0.2Hz, sinewave was always sharp up to a particular [?]K , before it started experiencing some significant blunting effect of the corrosion process. Note that the sharpness of crack tip ensured that the crack growth was not retarded. The blunting phenomenon may not have much retarding effect at very high [?]K because the crack driving force is enough to continually nucleate sharp crack fronts. In other words, the mechanical fatigue component leads the corrosion process in this domain. This suggests then that at the Paris Region, two domains appear to exist – corrosion dominated and mechanical-fatigue dominated domains. The corrosion-controlled domain appears to be strongly influenced by the $K_{\max}$ and time of crack tip exposure to the corrosive environment [67].

Fig. 19(a) is a typical nature of the crack path in the J2N steel in SW . Fig. 19(b) is a schematic of Fig. 19(a). The crack propagated with predominance of low angle crack-tip diversion, very limited low angle crack branching with the shorter arm in comparison with the $TMCP$ steels. The crack moved on a horizontal plane with minimal zig-zag motion. The crack growth pattern is generally the same with that of air (see Fig. 12(a)) except that the branched arms are shorter and there is widening of the crack gap as a result of the corrosion process. The branched crack tips are relatively blunted, but the main crack tip appeared to maintain its sharpness. No crumb formation was seen, and crack diversion and bifurcation are less than that in air. Hence, one would expect a very high $CFCGR$ for this crack growth pattern if blunting of the main active crack tip did not occur.

In Fig. 19, it appears that there is no predominant features of the phases influencing the crack growth, except that the crack diverted in a zig-zag manner which is a consequence of the crack propagation mechanism. A closer observation shows some influencing microstructural features. Some of the distinct micrographs showing phases and morphologies influencing the $CFCGR$ for the J2N are presented in Fig. 20. However, we could see that the branched crack tips appeared to be following the α/α and a/Π interfaces as shown by the arrows. In other words, the preferred crack paths appeared to be the α/α and α/P boundaries. The black arrow is the α/α while the blue arrow is the α/P. In fact, these boundaries are decorated by the ferrite phase ribbon of high alloy content and the crack followed the a_{HA} phase. We can also note the widening activity near and immediately behind the crack tip as it propagated. This is likely to be as a result of intense corrosion activity around the $microplastic$ zone.

Posted on Authorea 13 Apr 2020 — CC BY 4.0 — https://doi.org/10.22541/au.158679911.16268490 — This a preprint and has not been peer reviewed. Data may be preliminary.

Fig. 21 shows the comparison of the *FCGR* curves for the air and*SW* tests under sinewave and the experimental conditions are shown in Table 8. Fig. 21(a) shows that *CFCGR* of the 0.2Hz is higher than that of air by an average factor of 2.5 for the J2N steel. Above about 24 MPa[?]m, the rate increased up to an average factor of 4.0. These values are typical of normalised*α-Π* steels of the same microstructure. The sudden jump in the *CFCGR* to a factor of about 4 can be explained by examining the crack path in air and *SW* .

Table 8: Specimen dimensions and loading conditions in air and SW

#	Test ID.	W	B	a_o	a_f	f (Hz)	P_{max} (kN)
1	J2N-A10F5	50.00	16.00	20.50	29.53	5	10
2	J2N-S10F0.2	50.00	16.00	18.32	28.02	0.2	10
3	G8-A10F5	50.15	15.90	20.33	32.12	5	10
4	G10-A10F5	50.01	16.00	20.30	29.53	5	10
5	G10-S9F0.2	50.00	16.00	22.68	30.16	0.2	9
6	G10-S10F0.2	50.00	16.00	21.26	29.11	0.2	10
7	G10-S10F0.5	50.03	16.04	21.20	29.61	0.5	10
(in mm), R = 0.1	(in mm), R = 0.1	(in mm), R = 0.1	(in mm), R = 0.1	(in mm), R = 0.1	(in mm), R = 0.1	(in mm), R = 0.1	(in mm), R = 0.1

In air (Fig. 12), bifurcation, crumb formation and some zig-zag crack propagation were sustained to high [?]K . In the *SW* , at [?]K above the 24 MPa[?]m, the crumb formation and crack branching were almost absent (Fig. 19) and this resulted to a sudden increase in the *FCGR* to the factor of 4. In Fig. 21(b), the crack growth rates of the G8 and G10 denoted by the triangular data points, at 10kN, 5Hz are basically the same, confirming that the microstructures are similar. In the Paris Region taken from 19.50 MPa[?]m, the *CFCGR* is just higher than that of the air by a factor of about 1.5 measured from their respective mean lines (not shown). There is no obvious trend in the *CFCGR* s of the three tests in *SW* under sinewave in Fig. 21(b). We can reasonably say that the *CFCGR* s are the same above about 20.50 MPa[?]m, but below this value the 9kN, 0.2Hz test is somewhat higher. Fig. 21(c) shows the crack growth rates for the two microstructures – J2N and TMCP in air and *SW* . It is very clear that the crack path with the least crack diversion, branching and crumb formation gave the highest *FCGR* . The extent of these three phenomena is a function of the nature of the material microstructure and crack tip condition. If the microstructure, environment and loading condition are such that the three phenomena are extensive then crack growth retardation occurs - otherwise the rate may increase. High loading condition in *SW* tends to limit the extent of crack diversion and branching. This happens as a result of generation of relatively large plastically deformed areas around and ahead of the crack tip by the high loading condition and subsequent rapid dissolution of these areas by the electrochemical process resulting to various degrees of crack tip blunting. An incessant blunting of the crack front will limit the length of the diversion and branched arm, forcing the crack to propagate in a zig zag amplitude along the horizontal plane. Small zig zag amplitudes will increase the crack growth rate. This perhaps explains why the crack path found in J2N-A10F5 (Fig. 12) and J2N-S10F0.2 (Fig. 19) produced the highest crack propagation rate in air and *SW* respectively as shown in Fig. 21(c). In general, we observed that the crack path having considerable diversion, bifurcation and crumbs will lower the rate of the crack propagation. In Fig. 21(c), the *CFCGR* of the J2N is higher than that of *TMCP* steel by a factor of about 2.0 and this implies that the microstructure of the *TMCP* steel is superior to that of J2N in resisting crack growth in *α-Π* steel. Technologically, this implies that the microstructure of steel can be

Posted on Authorea 13 Apr 2020 — CC BY 4.0 — https://doi.org/10.22541/au.158679911.16268490 — This a preprint and has not been peer reviewed. Data may be preliminary.

engineered to retard *FCG* in the Paris Region!

We mentioned earlier that a general stress ratio, R = 0.1 has been used in this comparative study. This is an attempt to exclude the effect of the so-called crack closure, as if such effect exited it would affect the steels equally. In fact, the elimination of the asperities or rough edges makes roughness induced crack closure in corrosive environment unlikely. In the case of interlocking of deviated cracks, in *SW* the corrosion process will be rapid in these areas too because the mechanical rubbing action will exposure fresh surfaces for fast attack. Thus, the superiority of *TMCP* steels over the *NR* in *SW* , even in air cannot be attributed to crack closure and is unlikely for interlocking. A plausible reason in this study remains that under stress ratio range of 0.1 – 0.67, temperature range of 0°C to room temperature and frequency range of 0.05 – 0.7Hz, the microstructure of *α-Π* steel strongly affected the rate at which the crack propagated in air and *SW* in the Paris Region. This study therefore asserts that, the existing theory that the microstructure does not significantly affect the Paris Region appears to be incorrect. This tends to be so, when the same grade of steel, but with different phase morphologies are put into considerations. The major factor responsible for this difference appears to be the ferrite and pearlite phase morphologies and properties, which are function of the processing method and chemical composition of the steel.

Conclusions

This study investigated the influence of microstructure on the *FCGR* in advanced *α-Π* steels in the Paris Region, both in air and *SW* under sinewave fatigue loading. Three phenomena - crack diversion, crack bifurcation and metal crumb formation were identified as primary factors that retarded crack growth in the steels. The angle of crack-tip diversion and bifurcation affected the *FCGR* . The metal crumb affected *FCGR* by wedging action. The extent of formation of the three phenomena appears to be a function of the material microstructure, environment and crack-tip condition. If the microstructure, environment and loading condition are such that the three phenomena are extensive then crack growth retardation occurs - otherwise the rate may increase. That is, decrease in the crack diversion angle, branched-crack length and number of metal crumbs formed is found to increase *FCGR* . High angle crack-tip diversion, bifurcation and re-orientation of the metal crumb resulting to a mismatch or wedging action, retarded *FCG* . The three factors appear to retard the crack growth by reducing or re-distributing the effective stress or driving force at the main active crack tip. In *SW* , high angle crack diversion and bifurcation are considerably reduced and this is a consequence of the repeated crack tip blunting by the electrochemical dissolution process. If the branched crack tips are blunted such that the length is short and the main active crack tip is sharp, *CFCGR* can increase to about a factor of 4. If the main active crack tip is blunted as well, the crack propagation speed is considerably reduced. *Microplastic* zone appears to control *CFCGR* in *α-Π* steels. The *microplastic zone* size and the extent of the electrochemical dissolution of the zone (or crack tip blunting) appear to be additional primary factors influencing crack growth in *α-P* steel. The microstructural phases and morphology local to the main crack front and *microplastic* zone size appear to determine which mode the crack growth will adopt. The angle the crack front makes with the phases ahead of it tends to determine if it would propagate in transgranular or by *quasi-intergranular* mode under low *SIFR* . This study, therefore, asserts that the nature of the microstructures of the *α-P* steels has a strong influence on the *FCGR* in the Paris Region of the *da/dN* vs. [?]*K* sigmoidal curve in air and *SW* . However, considering the relatively small number of tests involved, more experiments are needed to confirm and increase the confidence in the results obtained in this work.

Acknowledgements

This work was supported by grant EP/L016303/1 for Cranfield, Oxford and Strathclyde Universities' Centre for Doctoral Training in Renewable Energy Marine Structures - REMS (http://www.rems-cdt.ac.uk/) from the UK Engineering and Physical Sciences Research Council (EPSRC).

Data availability: the raw data required to reproduce these findings cannot be shared at this time as the data also forms part of an ongoing study.

References

Posted on Authorea 13 Apr 2020 — CC BY 4.0 — https://doi.org/10.22541/au.158679911.16268490 — This a preprint and has not been peer reviewed. Data may be preliminary.

1. ASTM. ASTM E647-15: Standard test method for measurement of fatigue crack growth rates. 2015. Available at: DOI:10.1520/E0647-15.2

2. BSI. BS EN ISO 11782-2:2008: Corrosion of metals and alloys — Corrosion fatigue testing —Part 2: Crack propagation testing using precracked specimens. British Standard. 2008.

3. Ritchie RO. Near-threshold fatigue-crack propagation in steels. International Metals Reviews. 1979; 24(1): 205–230. Available at: DOI:10.1179/imtr.1979.24.1.205

4. Stonesifer FR. Effect of grain size and temperature on fatigue crack propagation in A533 b steel. Engineering Fracture Mechanics. 1978; 10: 305–314.

5. Milella PP. Fatigue and corrosion in metals. Milan: Springer-Verlag; 2013. 529–530 p. Available at: DOI:10.1007/978-88-470-2336-9

6. Zerbst U., Madia M., Vormwald M., Beier HT. Fatigue strength and fracture mechanics – A general perspective. Engineering Fracture Mechanics. Elsevier Ltd; 2018; 198: 2–23. Available at: DOI:10.1016/j.engfracmech.2017.04.03

7. Chen DL., Wang ZG., Jiang XX., Ai SH., Shih CH. The dependence of near-threshold fatigue crack growth on microstructure and environment in dual-phase steels. Materials Science and Engineering A. 1989; 108(C): 141–151. Available at: DOI:10.1016/0921-5093(89)90415-2

8. Liaw PK. Mechanisms of near-threshold fatigue crack growth in a low alloy steel. 1985; 33(8): 1489–1502.

9. Zerbst U., Vormwald M., Pippan R., Gänser H-P., Sarrazin-Baudoux C., Madia M. About the fatigue crack propagation threshold of metals as a design criterion–A review. Engineering Fracture Mechanics. 2016; 153(November 2014): 190–243.

10. Ritchie RO. Mechanisms of fatigue-crack propagation in ductile and brittle solids. International Journal of Fatigue. 1999; 100: 55–83.

11. Thompson AW., Bucci RJ. The dependence of fatigue crack growth rate on grain size. Metallurgical Transactions. 1973; 4(4): 1173–1175. Available at: DOI:10.1007/BF02645626

12. Lindigkeit J., Terlinde G., Gysler A., Lutjering G. The effect of grain size on the fatigue crack-Propagation behavior of age-hardened alloys in inert and corrosive environment. Acta Metallurgica. 1979; 27: 1717–1726.

13. Hoeppner DW. The effect of grain size on fatigue crack growth in copper. Fatigue Crack Propagation, ASTM 415. 1967; 18(STP415-EB/Jun): 489. Available at: DOI:10.1111/j.1460-2695.1995.tb00861.x

14. Francois D. The Influence of the microstructure on fatigue. In: Branco CM, Rosa LG (eds.) NATO ASI S. Advances in Fatigue Science and Technology; 1989. Available at: DOI:10.1016/B978-0-12-374364-0.50017-5

15. Laird C., Smith GC. Crack propagation in high stress fatigue. Philosophical Magazine. 1962; 7(77): 847–857. Available at: DOI:10.1080/14786436208212674

16. Pelloux RMN. Crack extension by alternating shear. Engineering Fracture Mechanics. 1970; 1(4). Available at: DOI:10.1016/0013-7944(70)90008-1

17. Stephens RI., Fatemi A., Stephens RR., Fuchs HO. Metal Fatigue in Engineering. 2nd edn. John Wiley & Sons. NY: John Wiley & Sons; 2001. 51 p. Available at: DOI:10.1115/1.3225026

18. Krupp U. Fatigue Crack Propagation in Metals and Alloys: Microstructural Aspects and Modelling Concepts. Weinheim: WILEY-VCH Verlag GmbH & Co; 2007. 136 p.

19. Elber W. Fatigue crack closure under cyclic tension. Engineering Fracture Mechanics. 1970; 2: 37–45. Available at: https://ac.els-cdn.com/0013794470900287/1-s2.0-0013794470900287-main.pdf?_tid=6de5a0ce-060b-43f9-adf5-6ddbc40eafbc&acdnat=1549818866_81d1eb651842856827206db98df61835

20. Elber W. The Significance of Fatigue Crack Closure. ASTM STP 486 - Damage Tolerance in Aircraft Structures. 1971; : 230–242. Available at: www.astm.org (Accessed: 10 February 2019)

Posted on Authorea 13 Apr 2020 — CC BY 4.0 — https://doi.org/10.22541/au.158679911.16268490 — This a preprint and has not been peer reviewed. Data may be preliminary.

21. Dillinger. Thermomechanically rolled fine-grained steels. 2016. Available at: https://www.dillinger.de/d/en/products/heav finegrained/ (Accessed: 11 April 2016)

22. Igwemezie V., Mehmanparast A., Kolios A. Materials selection for XL wind turbine support structures: A corrosion-fatigue perspective. Marine Structures. Elsevier; 1 September 2018; 61: 381–397. Available at: DOI:10.1016/J.MARSTRUC.2018.06.008

23. Steel International T. New Horizons - supply solutions in offshore structual steel. 2010. Available at: http://www.tatasteeleurope.com/static_files/StaticFiles/Business_Units/International/Tata Steel International Offshore Capability 2010.pdf (Accessed: 5 April 2016)

24. Corus Construction & Industrial. European structural steel standard EN 10025 : 2004. 2004. Available at: http://www.tf.uni-kiel.de/matwis/amat/iss/kap_9/articles/en_steel_standards.pdf (Accessed: 5 April 2016)

25. Tata Steel. Advance sections. 2013. Available at: http://www.tatasteeleurope.com/file_source/StaticFiles/section_-plates_publications/sections_publications/Advance to Eurocode Sept 13.pdf

26. Parker Steel Company. S355 EN 10025: Standard Structural Steel Products. 2012. Available at: http://www.metricmetal.com/products/Grade Descriptions/S355 Grade Description.php (Accessed: 1 April 2016)

27. Bhadeshia HKDH. Bainite in Steels - Transformation, Microstructure and Properties. 2nd edn. IOM Communications; 2001.

28. Meester B De. The Weldability of Modern Structural TMCP Steels. ISIJ International. 1997; 37(6): 537–551. Available at: DOI:10.2355/isijinternational.37.537

29. Tamura I., Sekind H., Taanaka T., Ouchi C. Thermomechanical processing of high-strength low-alloy steels. Butterworths; 1988. 248 p.

30. GRANGE RA. Fundamentals of deformation processing: proceedings. In: Backofen WA (ed.) Volume 9 of Sagamore Army Materials Research Conference proceedings. Syracuse University Press; p. 229. Available at: https://books.google.co.uk/books/about/Fundamentals_of_deformation_processing.html?id=QOg_-AQAAIAAJ&redir_esc=y (Accessed: 17 December 2018)

31. Fukumoto Y. New constructional steels and structural stability. Engineering Structures. Elsevier; 1 October 1996; 18(10): 786–791. Available at: DOI:10.1016/0141-0296(96)00008-9 (Accessed: 21 November 2018)

32. Shikanai N., Mitao S., Endo S. Recent Development in Microstructural Control Technologies through the Thermo-Mechanical Control Process (TMCP) with JFE Steel's High-Performance Plates. 2008. Available at: http://www.jfe-steel.co.jp/en/research/report/011/pdf/011-02.pdf (Accessed: 17 December 2018)

33. Bhadeshia HKDH. Interpretation of the Microstructure of Steels. Phase Transformation Group, University of Cambridge. Available at: http://www.phase-trans.msm.cam.ac.uk/2008/Steel_Microstructure/SM.html (Accessed: 9 October 2018)

34. Igwemezie VC., Ovri JEO. Investigation into the Effects of Microstructure on the Corrosion Susceptibility of Medium Carbon Steel. The International Journal Of Engineering And Science (IJES). 2013; 2(6): 2319–1805.

35. Slezak T., Sniezek L. A Comparative LCF Study of S960QL High Strength Steel and S355J2 Mild Steel. Procedia Engineering. 2015; 114: 78–85. Available at: https://ac.els-cdn.com/S1877705815016835/1-s2.0-S1877705815016835-main.pdf?_tid=a64b914d-b256-4bf1-bca8-3f2ab3afd688&acdnat=1547527288_d017f7cfa2d300a96252b52c (Accessed: 15 January 2019)

36. Igwemezie V., Dirisu P., Mehmanparast A. Critical assessment of the fatigue crack growth rate sensitivity to material microstructure in ferrite-pearlite steels in air and marine environment. Materials Science and Engineering A. 2019; 754: 750–765.

Posted on Authorea 13 Apr 2020 — CC BY 4.0 — https://doi.org/10.22541/au.158679911.16268490 — This a preprint and has not been peer reviewed. Data may be preliminary.

37. Steimbreger C. Fatigue of Welded Structures -Master thesis. Lulea University of Technology; 2014.

38. Korda AA., Mutoh Y., Miyashita Y., Sadasue T., Mannan SL. In situ observation of fatigue crack retardation in banded ferrite-pearlite microstructure due to crack branching. Scripta Materialia. 2006; 54(11): 1835–1840. Available at: DOI:10.1016/j.scriptamat.2006.02.025

39. Igwemezie V., Mehmanparast A. Waveform and frequency effects on corrosion-fatigue crack growth behaviour in modern marine steels. International Journal of Fatigue. 2020; 134. Available at: DOI:https://doi.org/10.1016/j.ijfa

40. Cheng YW. The fatigue crack growth of a ship steel in seawater under spectrum loading. International Journal of Fatigue. 1985; 7(2): 95–100. Available at: DOI:10.1016/0142-1123(85)90039-8

41. Musuva JK. PhD Thesis - Fatigue crack growth in a low-alloy steel. University of London; 1980. Available at: https://spiral.imperial.ac.uk/bitstream/10044/1/35278/2/Musuva-JK-1980-PhD-Thesis.pdf (Accessed: 27 September 2018)

42. De Jesus AMP., Matos R., Fontoura BFC., Rebelo C., Simoes Da Silva L., Veljkovic M. A comparison of the fatigue behavior between S355 and S690 steel grades. Journal of Constructional Steel Research. Elsevier Ltd; 2012; 79(August): 140–150. Available at: DOI:10.1016/j.jcsr.2012.07.021

43. Atkinson JD., Lindley TC. Effect of stress waveform and hold-time on environmentally assisted fatigue crack propagation in C-Mn structural steel. Metal Science. 1979; 13(7): 444–448. Available at: DOI:10.1179/msc.1979.13.7.444

44. Achilles RD., Bulloch JH. The influence of waveform on the fatigue crack growth behaviour of SA508 cl III RPV steel in various environments. International Journal of Pressure Vessels and Piping. 1987; 30(5): 375–389. Available at: DOI:10.1016/0308-0161(87)90110-4 (Accessed: 17 September 2018)

45. Barsom JM., Rolfe ST. Fracture and Fatigue Control in Structures : Applications of Fracture Mechanics, 3rd Edition. 3rd edn. ASTM; 1999. 318–323 p. Available at: DOI:10.1520/MNL41-3RD-EB

46. Barsom JM. Corrosion-fatigue crack propagation below KIscc. Engineering Fracture Mechanics. 1971; 3(1): 15–25. Available at: DOI:10.1016/0013-7944(71)90048-8

47. Musuva JK., Radon JC. The Effect of Stress Ratio and Frequency on Fatigue Crack Growth. Fatigue of Engineering Materials and Structures. 1979; 1: 457–470. Available at: https://onlinelibrary.wiley.com/doi/pdf/10.1111/j.1460 2695.1979.tb01333.x (Accessed: 14 October 2018)

48. Scott PM., Thorpe TW and., Silvester DR V. Rate-determining processes for corrosion fatigue crack growth in ferritic steels in seawater. Corrosion Science. 1983; 23(6): 559–575.

49. Appleton RJ. Corrosion fatigue of a C-Mn steel, PhD Thesis. Department of Mechanical Engineering, University of Glasgow; 1985. Available at: http://theses.gla.ac.uk/2176/ (Accessed: 13 February 2018)

50. Thorpe TW., Scott PM., Rance A., Silvester D. Corrosion fatigue of BS4360:50D structural-steel in seawater. International Journal of Fatigue. 1983; 5(3): 123–133.

51. Thompson JWC. PhD Thesis - Phenomenological investigation of the influence of Cathodic Protection on corrosion fatigue crack propagation behaviour, in a BS 4360 50D type structural steel and associated weldment microstructures, in a marine environment. Cranfield University; 1984.

52. Correia JAFO., Blason S., De Jesus AMP., Canteli AF., Moreira PMGP., Tavares PJ. Fatigue life prediction based on an equivalent initial flaw size approach and a new normalized fatigue crack growth model. Engineering Failure Analysis. 2016; 69: 15–28. Available at: DOI:10.1016/j.engfailanal.2016.04.003 (Accessed: 29 November 2018)

53. Adedipe O., Brennan F., Kolios A. Corrosion fatigue load frequency sensitivity analysis. Marine Structures. Elsevier Ltd; 2015; 42: 115–136. Available at: DOI:10.1016/j.marstruc.2015.03.005

Posted on Authorea 13 Apr 2020 — CC BY 4.0 — https://doi.org/10.22541/au.158679911.16268490 — This a preprint and has not been peer reviewed. Data may be preliminary.

54. Xiong Y., Hu XX. The effect of microstructures on fatigue crack growth in Q345 steel welded joint. Fatigue and Fracture of Engineering Materials and Structures. 2012; 35(6): 500–512. Available at: DOI:10.1111/j.1460-2695.2011.01640.x

55. Laurito DF., Baptista CARP., Torres MAS., Abdalla AJ. Microstructural effects on fatigue crack growth behavior of a microalloyed steel. Procedia Engineering. Elsevier; 2010; 2(1): 1915–1925. Available at: DOI:10.1016/j.proeng.2010.03.206

56. Callister DR. A study of fatigue crack propagation in quenched and tempered and controlled roller HSLA steels. Cranfield Institute of Technology; 1987.

57. Tsay LW., Chern TS., Gau CY., Yang JR. Microstructures and fatigue crack growth of EH36 TMCP steel weldments. International Journal of Fatigue. 1999; 21(8): 857–864. Available at: DOI:10.1016/S0142-1123(99)00021-3

58. Chapetti MD., Miyata H., Tagawa T., Miyata T., Fujioka M. Fatigue crack propagation behaviour in ultra-fine grained low carbon steel. International Journal of Fatigue. 2005; 27(3): 235–243. Available at: DOI:10.1016/j.ijfatigue.2004.07.004

59. Mehmanparast A., Brennan F., Tavares I. Fatigue crack growth rates for offshore wind monopile weldments in air and seawater: SLIC inter-laboratory test results. Materials and Design. 2017; 114: 494–504. Available at: DOI:10.1016/j.matdes.2016.10.070

60. Tavares I., Brennan F. The SLIC Project. 2015. Available at: http://www.ewea.org/offshore2015/conference/allposters/P

61. Li X., Cao L., Wang M., Du F. Groove design and microstructure research of ultra-fine grain bar rolling. Modeling and Numerical Simulation of Material Science. Scientific Research Publishing; 22 October 2012; 02(04): 67–75. Available at: DOI:10.4236/mnsms.2012.24008 (Accessed: 25 September 2018)

62. Saeed-Akbari A. Determination of steels microstructural components based on novel characterisation techniques. RWTH Aachen; 2008. Available at: DOI:10.1007/BF03192151

63. Adedipe O. Integrity of offshore structures. Cranfield University; 2015.

64. Kavishe FPL., Baker TJ. Effect of prior austenite grain size and pearlite interlamellar spacing on strength and fracture toughness of a eutectoid rail steel. Materials Science and Technology. 1986; 2(8): 816–822. Available at: DOI:10.1179/mst.1986.2.8.816

65. Callister WDJ. Materials Science and Engineering An Introduction. 7th (ed.) John Wiley & Sons, Inc; 2007. 226–227 p.

66. Daeubler MA., Thompson AW., Bernstein IM. Influence of microstructure on fatigue behavior and surface fatigue crack growth of fully pearlitic steels. Metallurgical Transactions A. 1990; 21A: 925–932. Available at: https://link.springer.com/content/pdf/10.1007%2FBF02656577.pdf (Accessed: 1 December 2018)

67. Igwemezie V., Mehmanparast A. Waveform and frequency effects on corrosion-fatigue crack growth behaviour in modern marine steels. International Journal of Fatigue. 2020; 134. Available at: DOI:10.1016/J.IJFATIGUE.2020.1

Posted on Authorea 13 Apr 2020 — CC BY 4.0 — https://doi.org/10.22541/au.158679911.16268490 — This a preprint and has not been peer reviewed. Data may be preliminary.